Atmos. Meas. Tech. Discuss., 3, 3199–3276, 2010
www.atmos-meas-tech-discuss.net/3/3199/2010/
doi:10.5194/amtd-3-3199-2010

Atmospheric Measurement Techniques Discussions

MAMAP – a new spectrometer system for column-averaged methane and carbon dioxide observations from aircraft: instrument description and performance assessment

K. Gerilowski[1], A. Tretner[2], T. Krings[1], M. Buchwitz[1], P. P. Bertagnolio[1,*], F. Belemezov[1], J. Erzinger[2], J. P. Burrows[1], and H. Bovensmann[1]

[1]University of Bremen, Institute of Environmental Physics, P.O. Box 330440, 28334 Bremen, Germany
[2]Helmholtz Centre Potsdam – GFZ German Research Centre for Geosciences, Telegrafenberg, 14473 Potsdam, Germany
[*]now at: University of Siena, Department of Earth Sciences, Via Laterina 8, 53100 Siena, Italy

Received: 9 July 2010 – Accepted: 13 July 2010 – Published: 2 August 2010

Correspondence to: K. Gerilowski (gerilows@iup.physik.uni-bremen.de)

Published by Copernicus Publications on behalf of the European Geosciences Union.

Abstract

Carbon dioxide (CO_2) and Methane (CH_4) are the two most important anthropogenic greenhouse gases. CH_4 is furthermore one of the most potent present and future contributors to global warming because of its large global warming potential (GWP). Our knowledge of CH_4 sources and sinks is based primarily on sparse in-situ local point measurements from micro sites and surface networks and more recently on low spatial resolution satellite observations. There is a need for measurements of the dry columns of CO_2 and CH_4 having high spatial resolution and spatial coverage. In order to fill this gap a new passive airborne 2-channel grating spectrometer instrument for remote sensing of small scale and mesoscale column-averaged CH_4 and CO_2 observations has been developed. This Methane Airborne MAPper (MAMAP) instrument measures reflected and scattered solar radiation in the short wave infrared (SWIR) and near-infrared (NIR) parts of the electro-magnetic spectrum at moderate spectral resolution. The SWIR channel yields measurements of atmospheric absorption bands of CH_4 and CO_2 in the spectral range between 1.59 and 1.69 µm at a spectral resolution of 0.82 nm. The NIR channel around 0.76 µm measures the atmospheric O_2-A-band absorption with a resolution of 0.46 nm. MAMAP has been designed for flexible operation aboard a variety of airborne platforms. The instrument design and performance, together with some results from on-ground and in-flight engineering tests are presented. The instrument performance has been analyzed using a retrieval algorithm applied to the SWIR channel nadir measured spectra. The signal-to-noise ratio (SNR) of the SWIR channel is approximately 1000 for integration times (t_{int}) in the range of 0.6–0.8 s for scenes with surface spectral reflectances of around 0.18. At these integration times the ground scene size is about $23 \times 33\,m^2$ for an aircraft altitude of 1 km and a ground speed of 200 km/h. For these scenes the CH_4 and CO_2 column retrieval precisions are typically about 1% (1 σ). Elevated levels of CH_4 have been retrieved above a CH_4 emitting landfill. Similarly the plume of CO_2 from coal-fired power plants can be well detected and tracked. The measurements by the MAMAP sensor enable estimates of

AMTD
3, 3199–3276, 2010

anthropogenic, biogenic and geological emissions of localized intense CH_4 and CO_2 sources such as anthropogenic fugitive emissions from gas industry and waste, emissions from coal-fired power plants or geologic emissions from seepage and volcanoes. Appropriate analysis of the measurements of MAMAP potentially also yields CH_4 emissions from less intense but extensive sources such as wetlands.

1 Introduction

Carbon dioxide (CO_2) and methane (CH_4) are the two most important anthropogenic greenhouse gases (GHG) contributing to climate change (IPCC, 2001, 2007; Wuebbles and Hayhoe, 2002). In addition CH_4 plays an important role in the chemistry cycle of the atmosphere (Rice et al., 2003; Wuebbles and Hayhoe, 2002; IPCC, 2001). Despite their importance, our knowledge about their natural and anthropogenic sources (and sinks) has significant gaps (IPCC, 2007; Wuebbles and Hayhoe, 2002). This arises in part because of the difficulty in estimating the highly variable natural and anthropogenic atmospheric source emissions in space and time (IPCC, 2001, 2007; Watson et al., 1990).

Up to now, flux estimates of CH_4 and CO_2 in current global, synoptic, and mesoscale 3-D chemical transport models (CTM) are based on either bottom-up or top-down approaches. For bottom-up flux estimates, microscale ground-based in-situ measurements are collated from a variety of different techniques, such as closed chamber and eddy covariance methods (Sachs et al., 2008, and references therein). Emission and flux estimates obtained by these techniques are assigned to specific soil/vegetation types and then are spatially extrapolated to meso and synoptic scales using, for example, a global vegetation index, which is derived from satellite imaging data (Takeuchi et al., 2003).

In contrast global, synoptic, and mesoscale, top-down emission estimates are based on precise atmospheric in-situ concentration measurements of the relevant gases from surface networks, tall towers, helicopters, aircrafts, and trains (Dlugokencky et al.,

AMTD
3, 3199–3276, 2010

1995, 2005; Winderlich et al., 2010; Matsueda and Inoue, 1999; Jagovkina et al., 2000; Oberlander et al., 2002; Nisbet, 2005; Miller et al., 2007; Kort et al., 2008). These measurements are then inverted to estimate flux rates between the surface and the atmosphere (Jagovkina et al., 2001; Chen and Prinn, 2006; Bergamaschi et al., 2005, 2007). Bottom-up flux estimates are often input into the inversion calculations. Based on the measured data the fluxes are modified during the inversion calculation (Chen and Prinn, 2006; Bergamaschi et al., 2005, 2007), in a way that the simulated atmospheric concentrations better match the observations. As a result of the coarse density of the surface observation site network, information about surface fluxes distant from the network is still not well defined and ambiguous (Villani et al., 2010; Bréon and Ciais, 2010).

With the launch of the European environmental satellite, ENVISAT, with the SCIAMACHY instrument on board (Bovensmann et al., 1999; Burrows et al., 1995), dry column averaged air mole fraction of CH_4, and CO_2, respectively XCH_4, and XCO_2, could be derived from space. The SCIAMACHY XCH_4 (Buchwitz et al., 2000, 2005a,b, 2006; Frankenberg et al., 2005; Schneising et al., 2009) and XCO_2 (Buchwitz et al., 2000, 2005a,b, 2006; Schneising et al., 2008) are retrieved from back scattered solar electromagnetic radiation in the Near Infrared, NIR, and Short Wave Infrared, SWIR, spectral regions. This radiation carries information about the absorption in the atmosphere and has high sensitivity to the boundary layer including the Earth's surface. These new remote sensing data were incorporated for the first time to estimate the annual CH_4 surface fluxes at a resolution of several degrees using top-down inverse modelling (Bergamaschi et al., 2007, 2009). Recently a new mission for GHG observations, the GOSAT satellite with the Tanso-FTS on board (Yoshida et al., 2008), was launched successfully in January 2009. The footprint of the Tanso-FTS instrument is 10 km with a gap of about 160 km between observations. Because SCIAMACHY's large typical footprint of 60 km×30 km, and the large gaps between the measurements of GOSAT single local emissions cannot be accurately resolved in the currently available satellite data (Bréon and Ciais, 2010). As a result of the high spatial and temporal uncertainty

AMTD
3, 3199–3276, 2010

and variability of anthropogenic, biological, and geological GHG sources on meso- and local scales, proper estimation of source strengths and their contribution to regional and global budgets from ground-based and satellite top-down modelling or simple bottom-up scaling remains inaccurate (Bréon and Ciais, 2010; Villani et al., 2010). In particular, the contribution of small "hot-spot" areas and single facilities is not sufficiently resolved with the existing observational systems.

For example, one poorly quantified CH_4 source exhibiting large temporal and spatial variability is on the Arctic shelf and slope, where a majority of the organic Arctic carbon pool is sequestered (Burlin and Sokolov, 2001). Large parts of this "Arctic carbon hyper pool" exist as gas hydrates primarily trapped under shallow relic marine permafrost (Gramberg et al., 1983). Based on 2003–2008 East Siberian Arctic Shelf (ESAS) data (the only Arctic shelf with long-term CH_4 emission monitoring) the subsea permafrost over vast areas is increasingly permeable with more than 80% of the ESAS seabed being a CH_4 source (Shakhova et al., 2007, 2010). In-situ measurements of ship-based transects show local atmospheric concentration increases of up to 8 ppmv (Shakhova et al., 2007). Increases in subsea permafrost permeability and seepage occurring throughout all shallow Arctic Seas are anticipated but not yet confirmed. Due to its vast stored carbon reserves (probably the largest on the planet) (Gramberg et al., 1983) mostly sequestered and submerged by increasingly permeable permafrost, the rapidity of climate change and decrease of permafrost in Arctic regions, has a large potential to alter global climate (Archer and Buffett, 2005). Here, satellite and airborne remote sensing measurements could play a critical role in evaluating emissions.

Another poorly quantified, highly variable CH_4 source was discovered by Walter et al. (2006, 2007), who found evidence for a two to three times higher emissions of CH_4 bubbling from thaw lakes located in the North Siberian permafrost areas, than calculated in other studies. Global CH_4 release from wetlands in the tropical and northern regions (including thaw lakes in permafrost areas) have been estimated to contribute from about 20% (100 of total 500 Mt CH_4/yr, Wuebbles and Hayhoe, 2002) to about 24% (145 of total 596 Mt CH_4/yr, Chen and Prinn, 2006) of the global natural CH_4

AMTD
3, 3199–3276, 2010

emissions. Walter et al. (2007) bottom-up extrapolated the measured thaw lake fluxes to all lakes north of 45° N suggesting that northern lakes emit 24.2 ± 10.5 Mt CH_4/yr. This has not yet been included in global estimates (Walter et al., 2007). It is expected that global warming will lead to significant increases in CH_4 emissions from thawing permafrost areas (Fung et al., 1991; Bartlett and Harriss, 1993; Khalil, 2008; Walter et al., 2007). On the other hand, northern wetlands emissions (from 30–90° N) have been estimated by surface network and satellite top-down modelling to be responsible for 42.5 Mt CH_4/yr rather than the initial (bottom-up) estimate of about 59.5 Mt CH_4/yr of global models (Bergamaschi et al., 2007). This is significantly smaller than the total annual wetland emissions of 175 Mt CH_4/yr used as apriori input for that model.

Also geological CH_4 sources, including mud volcanoes and marine and terrestrial hydrocarbon seepage, represent an important, yet poorly quantified source (Mörner and Etiope, 2002; Etioppe and Klusman, 2004; Etiope et al., 2004, 2007; Etiope, 2009). Bottom-up estimates for natural global geological CH_4 emissions are in the range of 30–45 Mt CH_4/yr (Etioppe and Klusman, 2002), which are estimated to contribute 43% of the natural CH_4 European emissions (Etiope, 2009). Other bottom-up studies (Dimitrov, 2002) suggest that 0.36 to 1.6 Mt CH_4 enters the atmosphere every year only from gas seeps on the Black Sea continental shelf, less than 0.5% of the world's total continental shelves. Currently, geological CH_4 emissions are not yet, or only partially considered, in global estimates (Etioppe and Klusman, 2004; Chen and Prinn, 2006).

In addition to our limited knowledge about the magnitude and uncertainties of the above geological CH_4 emissions, accurate global estimates of CO_2 fluxes from geological sources such as subaerial volcanic degassing are required, especially with respect to intraplate and alkaline volcanism (Mörner and Etiope, 2002). The total atmospheric impact from global volcanic CO_2 degassing with 300 Mt/yr (Mörner and Etiope, 2002) is small compared to anthropogenic sources (26 000 Mt/yr Watson et al., 1990), but, up to now, measurements or rough estimates of CO_2 emission rates have been assessed for less than 20 volcanoes, compared to the 165 subaerial volcanoes that erupted in the period 1980–1989 (Mörner and Etiope, 2002). Estimates of CO_2 emissions of

AMTD
3, 3199–3276, 2010

alkaline volcanoes like Mount Etna show that emission rates of up to 25 Mt CO_2/yr are not infrequent. It has been recognized recently that the quiescent, non-eruptive diffuse degassing is the principal mode of gas release from volcanoes, thus, volcanic flank emissions can play a fundamental role in the volcanic carbon budget. For example, the total flux from soil degassing and fumaroles for Vulcano Island (Italy) is three times larger than emission estimates from the crater based on in-situ airborne measurements (Baubron et al., 1990; Chiodini et al., 1996; Italiano et al., 1998).

Flux estimates of strong micro scale CH_4 sources such as landfills, waste sites, or fugitive emissions from fossil fuel production industry vary considerably. For example, landfill CH_4 fluxes to the atmosphere have been estimated to be about 61 Mt CH_4/yr (Wuebbles and Hayhoe, 2002) using primarily closed chamber methods and model calculations. As a result of the high spatial variability, Börjesson et al. (2000) found that, for the same landfill, CH_4 emissions were a factor of 4 higher, when estimated using a tracer gas technique, than that estimated from closed chamber measurements (41 kg CH_4/h for the tracer method versus 9.7 kg CH_4/h for the closed chamber method). He concluded, that static chambers flux measurements cannot be trusted for more than small-scale bottom-up estimates of landfill gas emissions. Discrepancies have also been observed in comparisons between Differential Absorption Lidar (DIAL) remote measurements of fugitive emissions from natural gas plants and same emissions calculated by bottom-up emission factors (Chambers and Strosher, 2006a). Chambers and Strosher (2006a) reported a factor of 4–7 higher CH_4 emissions for two different natural gas processing plants when measured with ground based DIAL than calculated by emission factors of the single components (1264 and 1020 t CH_4/yr measured with DIAL versus 188 and 251 t CH_4/yr calculated by emission factors). Similar results also were obtained from DIAL measurements of fugitive CH_4 emissions of a Canadian oil refinery (Chambers and Strosher, 2006b), where emissions measured with ground based DIAL were up to 9 times higher than that calculated by bottom-up emission factors estimates (2400 t CH_4/yr measured with DIAL versus 258 t CH_4/yr calculated by emission factors). Although fugitive oil and gas industrial emissions have

AMTD
3, 3199–3276, 2010

been estimated to account for about 60 Mt CH_4/yr of global CH_4 emissions (Wuebbles and Hayhoe, 2002), the majority of these estimates are based on simple bottom up emission factor estimates such as that made for the entire Barnett Shale area (Armendariz, 2008). The accuracy of such assessments is questionable.

All these deficiencies in our knowledge of point sources and "hot-spot" areas demonstrate a clear need for the development of new measurement techniques to improve top-down estimates and constrain strong local emissions. These techniques are needed to extend the coverage and facilitate the integration of existing global systems and address the up-scaling issue. In this respect, airborne passive and active remote sensing techniques offer potentially a unique set of opportunities, as they combine range with high spatial resolution.

Until recently, few airborne instruments have had the capability of measuring CH_4 atmospheric columns with the high spatial resolutions ($\ll$250 m) and sufficient precision and accuracy (i.e. of equal or better ~1–2% CH_4 total atmospheric column), required for "hot-spot" detection for a range of important local and mesoscale atmospheric applications (see Sect. 5). Successful examples are DIAL instruments intended for pipeline leakage detection and monitoring (Meyer et al., 2006; Zimig and Ulbricht, 2006; Ershov, 2007) or instruments based on passive absorption techniques (Suto et al., 2008; Meyer et al., 2006; Roberts et al., 2010). Currently, information for comparisons between different active LIDAR systems and passive instruments are not readily available. For a realistic comparison, parameters such as threshold sensitivity, pulse repetition rate, total measurement time, distance from target, and measurement conditions are required. Nevertheless, it is reported that active DIAL instruments reach a threshold sensitivity during flight at typical flight altitudes of 100 m in the range of 80 ppm m[1] (for ground based laboratory measurements) (Meyer et al., 2006) and 100 ppm m (airborne at 0.5 s measurement time) (Ershov, 2007). Reported measure-

[1] ppm m is the atmospheric mixing ratio (in ppm) measured by the instrument multiplied by the equivalent atmospheric absorption light path calculated for standard conditions of temperature and pressure.

AMTD
3, 3199–3276, 2010

ments of all active systems have been limited to about 300 m altitude, which is not appropriate for many applications requiring minimal ranges of operation equal to the height of the planetary boundary layer (up to 2000 m). Model calculations show, that strong CH_4 concentration gradients occur up to altitudes of 7000 m (Jagovkina et al., 2001). Recent developments of high altitude CH_4 LIDAR based airborne demonstrators for active satellite missions are ongoing but not yet available for field application. In contrast to active DIAL systems, altitude limitations have less impact on passive airborne systems measuring in the short wave infrared (SWIR) spectral region. Working with back scattered solar electromagnetic radiation in the SWIR has the advantage that this radiation primarily is scattered from the earth's surface yielding high sensitivity in the boundary layer, where the concentration is maximum (Bréon and Ciais, 2010). In contrast, passive instruments using CH_4 and CO_2 absorption bands in the TIR (i.e. mid wave infrared and long wave infrared) have decreased surface sensitivity with increasing altitude due to the fact, that thermal electromagnetic radiation radiates both from the ground and from higher atmospheric layers (Bréon and Ciais, 2010; Crevoisier et al., 2009; Yoshida et al., 2008). The higher the instrument is flown, the smaller is the sensitivity to the lower parts of the boundary layer (Bréon and Ciais, 2010). On the other hand, passive SWIR/NIR systems (<2.4 µm) are limited to daytime, clear sky cloud free conditions, and appropriate solar zenith angles (SZAs).

Passive airborne remote instruments for CH_4 detection outside the TIR are rare. To the best of our knowledge, only three systems exist. One is used as the passive part of an airborne gas leakage detection system (Meyer et al., 2006). The system is based on a compact 1/4 m polychromator working in the 1.60 µm to 1.68 µm spectral range and has a detection limit of 800 ppm m (ca. 5% total column, referred to a 1013 hPa normalized total atmospheric thickness of about 8580 m, see Sect. 4.3.4) (Meyer et al., 2006). The second system is an airborne SWIR FTS developed for GOSAT validation and calibration (Suto et al., 2008). For this system "in-flight" detection limits have not been yet published. Roberts et al. (2010) reported recent successful trials adapting retrieval algorithms for the hyperspectral imaging data of the Airborne Visible Infrared

AMTD
3, 3199–3276, 2010

Imaging Spectrometer (AVIRIS) to map CH_4 emissions over strong marine geological CH_4 sources. For AVIRIS glint measurements over water surfaces with known properties of spectral reflectance theoretical detection limits for the resulting CH_4 maps of 36 ppb CH_4 total column increase (corresponding to 300 ppm m) for surface spectral reflectances SSR>0.22 are reported. For smaller SSR (i.e. <0.22) the detection limit degrades proportionately with the decreasing radiance (Roberts et al., 2010). It is expected that CH_4 retrieval from terrestrial, low spectral resolution, hyperspectral data is much more demanding as a result of the need to model accurately the SSR to reduce the uncertainty in the retreived CH_4 columns.

In order to improve our understanding of CH_4 and CO_2 sources (and sinks) and their variability at micro and meso scales by using top-down constraints and to validate space-based measurements on meso and synoptic scales (i.e. from SCIAMACHY and GOSAT), new measurement systems are needed. These must be capable of measuring CH_4 from high altitudes (>7 km) over different surface types at high horizontal resolution (<250 m) over areas <10 km up to 200 km and yield a precision and accuracy equal or better than the accuracy achieved by current and planned sensors, i.e. with a precision and accuracy of equal or better than about 1–2% (Bréon and Ciais, 2010). Such a system will need to resolve (strong) local fluxes (see Sect. 5) and link in-situ point measurements and flux estimates with micro and meso scale data from the local up to synoptic scale satellite measurements to address the up-scaling issue. The measured data ideally needs to be of an accuracy and precision to yield on inversion the CH_4 emissions from less intense but extensive and larger scale sources and sinks, such as wetlands. As a threshold the accuracy and precision of the data yields on inversion significant constrains on local hot spot emissions to separate them from the less intense but extensive larger scale sources and sinks and thereby allowing an improved estimate of both.

To address the evolving and emerging need not accommodated by other instruments, a team from the University of Bremen and the Helmholtz Centre Potsdam, German Research Centre for Geosciences (GFZ), have developed an airborne

AMTD
3, 3199–3276, 2010

spectrometer system, capable of direct and quantitative remote column-averaged measurements of atmospheric CH_4 and CO_2. This system, named the "Methane Airborne MAPper" (MAMAP), is designed for flexible operations on a variety of airborne platforms, and is described in detail below. MAMAP is equipped with a down-looking telescope for nadir observations and an up-looking light inlet for zenith observations. The MAMAP aircraft instrument was designed to measure total vertical columns of CH_4 and CO_2 on small spatial scales with a precision and relative accuracy equal or better than 1–2% (threshold <2%, target <1%) over land for typical albedo/SSR of about 0.18. This corresponds to a column enhancement of the concentration of about 150–300 ppm m below the aircraft which places limitations on the measurable target emission strengths (see Sect. 5).

The instrument is designed to operate at altitudes of more than 20 km from pressurized cabins and up to 4 km in non-pressurized cabins allowing measurements to above the convective boundary layer (CBL). Furthermore, it achieves a ground scene size of <300 m (along the flight track) on high altitude aircrafts with cruise speeds around 900 km/h. Depending on cruise speed, pixel sizes range typically between <50 and 150 m on slower (<400 km/h) propeller aircrafts (see Sect. 2).

This manuscript is organized as follows: In Sect. 2 the MAMAP instrument is described and its specifications are given. The current version of the MAMAP retrieval algorithm, which has been used to assess the on-ground and in-flight instrument performance, is briefly explained in Sect. 3. In Sect. 4 the results of the MAMAP instrument performance analysis are presented and discussed. In Sect. 5 relevant CH_4 and CO_2 emission targets are discussed. In Sect. 6 first results are shown from the analysis of flights near or over anthropogenic CO_2 and CH_4 emission sources. Finally, a summary is given in Sect. 7.

AMTD
3, 3199–3276, 2010

2 Description of the MAMAP instrument

The MAMAP instrument comprises two thermally stabilized grating spectrometer systems having a focal length of F=300 mm and a f-number of f/3.9. One spectrometer system measures in the SWIR over the spectral region at 1590–1690 nm to enable simultaneous retrieval of CO_2 (1590–1620 nm) and CH_4 (1630–1750 nm) columns. The second push-broom imaging spectrometer system measures in the NIR over the spectral region between 756–769 nm for the detection of the oxygen (O_2) absorption using the O_2-A band. The retrieved O_2 columns can be used to convert the greenhouse gas columns into dry-air column-averaged mixing ratios (see Sect. 3).

Both spectrometers have two independent telescopes, collecting electromagnetic radiation, and pointing towards nadir and upwards to the zenith-sky direction (Figs. 1 and 2). A fold-mirror allows switching between the nadir and zenith-sky modes of operation. This permits sequential measurement of the diffuse up-welling and down-welling radiance. Optionally, cosine diffuser plates or a combination of cosine diffuser plates plus glass fibres and collimator optics can be installed on-top of the zenith sky telescopes. In this configuration the instrument can perform direct solar irradiance measurements and diffuse down-welling (ir)radiance measurements in zenith-sky mode. From these measurements total and/or partial vertical columns can be retrieved as will be described in Sect. 3.

2.1 The CH_4/CO_2 SWIR spectrometer

A single grating SWIR spectrometer is utilized to simultaneously retrieve CH_4 and CO_2. This spectrometer uses a special F=300 mm modulation transfer function (MTF) optimised aspheric doublet lens (manufactured by ZEISS) for nadir observations and a single spherical lens (F=300 mm) for zenith-sky observations. The instantaneous field of view (IFOV) of the SWIR spectrometer is 1.34° across track (CT) and 0.02° along the flight track (LT).

AMTD
3, 3199–3276, 2010

The sensor head of the SWIR spectrometer is a modified linear photodiode array camera from Princeton Instruments (OMA-5, LN-1024) using a linear extended InGaAs 1024 pixel focal plane array (FPA) as detector. The detector is cooled with liquid nitrogen to −120 °C to minimise detector noise. With a pixel pitch of 25 µm, this array covers 25.6 mm in the spectral direction of the spectrometer's focal plane. In combination with a 600 grooves/mm spectrometer grating, a spectral window of 97.3 nm can be covered with a spectral resolution of about 0.82 nm (FWHM). At this resolution a sampling of approximately 8.6 detector pixels per FWHM is achieved. The coverage of a 97.3 nm spectral window permits the simultaneous measurement of CH_4 and CO_2 absorption bands with the same detector.

The dark signal of the sensor was reduced from ~600 fA to below 60 fA measured at an optical bench temperature of 25 °C by modifying the camera head. With the full well capacity of a single detector pixel of about 4.4 Me^- this dark signal reduction yields a theoretical signal to noise ratio (SNR) of 1000 and higher over land (surface albedo/SSR=0.18, detector exposure time t_{exp}~0.6 s) and a SNR of larger then 350 over water (albedo/SSR ~0.01, t_{exp}~3–5 s). Details concerning the SNR estimates are given in Sect. 4. To prevent detector saturation for high albedo/SSR scenes at nominal operation, the exposure time for a single readout is typically reduced by a factor of 10 (from 580 ms to 58 ms) over land and to 1–2 s over water. Over land, bursts of typically 10 single detector-readouts are collected and stored. All single readouts of each burst are then co-added in order to reach an appropriate SNR. This mode of operation is referred to as "co-added burst mode". For a flight altitude of 1 km, a surface albedo/SSR of 0.18 and a flight speed of ~200 km/h (e.g., Cessna 207 aircraft), a co-added ground pixel size of 23.4 m (cross track, CT) × 33 m (along track, LT) can be achieved for a total co-adding/integration time of ~0.6 s.

2.2 The O_2-A-band NIR spectrometer

A push-broom imaging NIR spectrometer system, operating in the 756 to 769 nm spectral range detects O_2. It uses two F=80 mm lens doublets for nadir and zenith sky

AMTD
3, 3199–3276, 2010

operation.

The IFOV is 5.85° (CT)×0.072° (LT). In the CT direction, the IFOV is approximately 4 times larger than the IFOV of the SWIR spectrometer. This larger IFOV was chosen to allow characterization of the surrounding scene. In imaging direction (CT) the NIR IFOV is subdivided in 85 discrete pixels. During post processing, approximately 1/4 of these 85 detector pixels is software binned to a window for each detector reading. In this manner, a single 1-D-spectral readout can be created which can be matched to the IFOV of the (1-D) SWIR spectrometer. To optimally match both IFOV (see Fig. GEOM) the binned NIR-IFOV window can be moved in CT direction during post processing, until optimum co-alignment to the SWIR IFOV is achieved. Due to both spectrometers small IFOV in the LT (i.e., flight) direction, the LT pixel size is defined primarily by the total co-adding/integration time of each burst. Sufficiently good LT synchronisation of the pixels for both spectrometers is achieved by electronic synchronisation of the exposure times and the detector readouts.

The NIR O_2-A spectrometer system uses an E2V 512×512 pixel frame transfer (FT) CCD with a pixel pitch of 16 µm×16 µm as detector. The detector is cooled to −30 °C by thermoelectric coolers, to minimise the detector noise. To speed up the readout time and reduce the data output, 6 pixels in imaging and 2 pixel in spectral direction are hardware binned, resulting in an array of 85 (spatial) and 256 (spectral) pixels with a pixel size of 96 by 32 µm. The readout of the FT-CCD is fully hardware synchronized with the readout of the SWIR detector by trigger pulses. The FT-CCD covers 8.192 mm×8.192 mm of the – push-broom – imaging spectrometers focal plane. In combination with a 1200 grooves/mm spectrometer grating, a spectral window of 13 nm can be imaged on the detector, resulting in a spectral resolution of ∼0.46 nm (FWHM). With the (binned) pixel size of 32 µm (in spectral direction) a sampling of ∼9 pixels per FWHM is achieved. Respectively, hardware binning of 6 pixels in imaging direction, divides the NIR spectrometers field of view in the mentioned 85 pixels (CT). For an albedo/SSR of ∼0.18, detector fillings in the range of 50–70% are achieved for an exposure time of ∼0.6–0.8 s. With the full well capacity of 1560 ke^- for a single hardware

AMTD
3, 3199–3276, 2010

binned (6×2) detector pixel, theoretical SNR values of ∼1000 per (binned) pixel can be achieved. In order to prevent detector saturation for high albedo/SSR scenes, the single readout exposure time is also reduced by a factor of 10 (as for the SWIR detector). Thus, a typical burst of 10 single detector-readouts are collected and stored (and later co-added).

The (6×2) binned pixel SNR was further increased by additional binning in across flight direction on the cost of spatial resolution. For example, CT software binning of all pixels of the NIR channel within the IFOV of the SWIR channel (i.e. ∼1/4 of the 85 NIR spectrometer pixels, see Fig. 3), will result in a theoretical SNR of more than 4000.

2.3 Pointing and image navigation

To monitor the position and the pointing of the instrument, MAMAP is equipped with a Garmin 5 Hz GPS and a Microstrain 3DM GX1 gyro-system. The readout of the position data of both devices is fully synchronized with the readout of the spectrometers. Additional position logging systems can be synchronized to MAMAP via external triggers. The MAMAP system also contains a triggered 640×480 pixel 1/4″ interline CCD colour camera (type: DFK 21BF04) for image acquisition which is synchronized with the spectrometer sensors. The CCD camera is equipped with a 25 mm lens and has the IFOV of 7.2° (CT)×5.7° (LT). This optical control helps to optimise the pointing knowledge of the MAMAP system. In this manner, pointing information towards different ground surface types can link CH_4 and CO_2 column information with potential CH_4 or CO_2 sources.

2.4 System control, data acquisition and power supply

Each SWIR and NIR spectrometer system uses a separate ultra slim, fan-less Advantech S123T panel PC for data acquisition, management of housekeeping data and the spectrometer (zenith/nadir) fold mirror control. For control and data acquisition of the CCD camera, the GPS and the gyro system, a separate embedded PC is used.

AMTD
3, 3199–3276, 2010

To avoid data damage over 3000 m flight altitude in unpressurised aircraft cabins all computers were equipped with flash disk devices for data storage. Thermal stabilization of the system was performed by two "off the shelf" digital PID controller units in combination with thermoelectric heaters. The system is powered through an uninterruptible power supply (UPS) and an optional 28 V DC to 220 V AC converter permitting the instrument to be operated either on 28 V DC or 220 V AC. The UPS has a GILL 28 V/43 Ah sealed lead acid battery, allowing the instrument to be operated up to 2 h without external power.

The whole system including all controllers and the battery-buffered power supply fits into two standard (DLR-Falcon) aircraft racks (556 mm×650 mm×968 mm each). The weight of each rack is approximately 120 kg. The first rack contains the camera controllers, the spectrometers and telescopes with the thermal control unit. The second rack contains the panel and the embedded PC's for the spectrometer control and data acquisition and the UPS system (Fig. 4). It has to be noted that MAMAP is currently not optimised w.r.t. mass, and there is potential for some significant mass reductions if required.

The instrument has been designed for flexible operation on-board a variety of airborne research platforms (e.g., Dornier 228, Dassault Falcon, Cessna Caravan, Basler-DC3 Polar-5 etc.) and provides all needed synchronisation signals for external Gyro and GPS logging systems. The sensor parameters are summarised in Table 1.

3 MAMAP retrieval algorithm and the determination of data products

The objective of the retrieval algorithm is to invert MAMAP spectra to derive the CH_4, CO_2 and O_2 – total or partial – vertical columns and the CH_4 and CO_2 column-averaged dry air mixing ratios, XCO_2 and XCH_4. For the retrieval, measurements of dark signal and pixel to pixel gain corrected (nadir) radiance spectra are used. The measurements and the target quantities being similar with those of the SCIAMACHY satellite instrument on ENVISAT (Buchwitz et al., 2005a,b; Schneising et al., 2008, 2009).

AMTD
3, 3199–3276, 2010

The derivation of the absolute column amounts (in units of number of molecules per unit area, e.g., molecules/cm^2) into column-averaged dry air mixing ratios (in ppm for CO_2 and ppb for CH_4) requires knowledge of the corresponding "dry air column", i.e. the total number of molecules in the observed atmospheric column, neglecting water molecules. For the interpretation of the MAMAP measurements the column-averaged mixing ratios are the preferred to the absolute columns, because of their much weaker dependence on the changes of surface topography/pressure and flight altitude. There are several approaches to estimate the dry air column needed for the conversion of the greenhouse gas columns into column-averaged mixing ratios:

(i) by the use of the simultaneous measurements of the oxygen (O_2) column retrieved from spectral measurements of the O_2-A band (located at 760 nm) analog to the method described in Schneising et al. (2008), for SCIAMACHY column-averaged CO_2 retrieval,

(ii) by using another, well mixed gas whose mixing ratio is well enough known and varies less than the trace gas of interest (e.g. by using the simultaneously retrieved CO_2 column for normalizing the retrieved CH_4 columns to obtain the column averaged mixing ratio of CH_4, Frankenberg et al., 2005; Schneising et al., 2009), and

(iii) by using external information on surface pressure obtained from, e.g., meteorological analysis by analogy to the method described in (Barkley et al., 2006), for column-averaged CO_2 retrieval.

The advantage of the first approach is that the mixing ratio of O_2 in dry air is well known (20.95%) and constant up to about 100 km and comprises 99.99% of the atmosphere. However, differences in the radiative transfer of the electromagnetic radiation through both absorption and scattering result in the path of radiation through the atmosphere being dependent on wavelength. Consequently, the presence of scattering by aerosols, cirrus or other clouds, gives a somewhat different light paths around 760 nm in comparison to 1.6 µm, as the phase function for particle scattering depends on wavelength (see

AMTD
3, 3199–3276, 2010

Schneising et al., 2008, 2009; Schneising, 2009, for a discussion of this approach). In order to use the O_2 band for the determination of XCO_2 and XCH_4 scattering needs to be explicitly accounted for.

An alternative approach for the determination of XCH_4 at least in regions where diurnal or spatial CO_2 variations are small is to assume that the CO_2 is effectively constant and well mixed compared to CH_4. As the relevant relatively weak absorptions of both gases occur spectrally close to one another, the path of the electromagnetic radiation is approximately identical for CO_2 and CH_4. For this reason, one of the XCH_4 data products is retrieved from SCIAMACHY (Frankenberg et al., 2005; Schneising et al., 2009) in this way. For this approach to be valid for the scene, CO_2 must be significantly less variable than CH_4. For the SCIAMACHY's large ground pixel size (30 km×60 km) this is reasonable, but could be problematic for the much smaller MAMAP ground pixel size. In summary all three methods can be used for MAMAP. The method, which performs best, depends on the target and the validity of the assumptions and the effort made to account for cloud and aerosol within the retrieval algorithm.

In this manuscript we focus on results obtained in the SWIR (1.6 nm) channel of MAMAP. To assess the instrument performance we have developed an initial version of a retrieval algorithm for MAMAP. In the following we present a short characterization of this algorithm. A more detailed description will be given elsewhere (Krings et al., 2010).

The MAMAP retrieval algorithm, used in this study, is derived from the Weighting Function Modified Differential Optical Absorption Spectroscopy (WFM-DOAS) retrieval algorithm (Buchwitz et al., 2000), referred to as the WFMD/M retrieval algorithm. The WFM-DOAS retrieval algorithm has been developed for and applied successfully to the retrieval of CH_4 and CO_2 vertical columns from SCIAMACHY nadir spectra (Buchwitz et al., 2005a,b; Schneising et al., 2008, 2009). Similar to WFM-DOAS, the WFMD/M retrieval algorithm uses a least-squares fitting procedure to minimise the difference between the logarithm of a simulated radiance spectrum with that measured. The simulated spectrum and the derivatives ("Jacobians") of this spectrum with respect to

AMTD
3, 3199–3276, 2010

a change of atmospheric parameters (mainly scaling factors for the CH_4, CO_2 and H_2O vertical profiles and temperature profile shift) are computed with the radiative transfer model (RTM) SCIATRAN (Rozanov et al., 2005) using the HITRAN data base (Rothman et al., 2005) and the solar spectrum from Livingston and Wallace (1991). These derivatives are called weighting functions. In addition to the geophysical fit parameters, a low order polynomial in the spectral domain is used to account for all smoothly varying spectral parameters, which are not explicitly modelled or inadequately known. These parameters include, for example, the MAMAP absolute radiometric calibration function, aerosol scattering, and absorption parameters and the surface spectral reflectance.

Figure 5 shows an example result for a WFMD/M analysis of a single spectrum, recorded by the MAMAP SWIR channel. The absorption features of CH_4 (Fig. 5 left) and CO_2 (Fig. 5 right) are clearly visible in the MAMAP spectrum. Interfering gases in the CH_4 fitting window (left) are CO_2 and H_2O. In the CO_2 fitting window (right) only H_2O interferes. Also fitted is the shift of the temperature profile (only shown for the CO_2 fitting window). The retrieved CH_4 profile scaling factor (PSF) is 0.989 ± 0.014. The retrieved CO_2 PSF is 0.991 ± 0.022. The residual ("RES") is shown in the bottom panels and is the difference between the MAMAP spectral measurements and the fitted radiative transfer model. The root-mean-square (RMS) of the residual is ~0.6% for both fitting windows. As can be seen, the fit residual is not only determined by measurement noise but also contains systematic features. This is currently attributed to wavelength calibration errors, slit function uncertainties, uncertainties of the spectroscopic line parameters or spectral structures of the white lamp calibration source.

As a result of the correlation between weighting functions of different altitude layers, the MAMAP retrieval is not height sensitive and weighting functions are integrated over the entire profile. Thus, the retrieval output PSF always indicates an altitude averaged change in the column concentration. For example a PSF of 1.01 means that the retrieved column is 1% higher than the vertical column which has been assumed for the radiative transfer simulations. During a flight of the MAMAP instrument, significant concentrations changes are expected below the aircraft, resulting from significant changes

AMTD
3, 3199–3276, 2010

in surface emission fluxes. Inspection of the averaging kernels (Fig. 6) shows a striking difference of about a factor of two below and above the aircraft. This difference is explained by the fact that for a nadir viewing instrument electromagnetic radiation coming from the sun passes through the absorber below the aircraft twice: once before and once after surface reflection (or surface scattering). SCIATRAN accounts for this path doubling in the weighting functions for each layer. The current retrieval algorithm only uses the co-added weighting functions from all height layers. Hence a column averaged PSF will always overestimate the real concentrations in the total column, because the averaged weighting functions are smaller than the weighting functions below the aircraft. To account only for an increase or decrease in CO_2 and CH_4 concentrations compared to background below the aircraft while leaving the column above unchanged, the original profile scaling factors (PSF) is multiplied by a conversion factor c (Table 2) derived from RTM simulations. The resulting new column scaling factor (CSF) as the scaling factor for the total column increase or decrease, assuming that all changes in concentrations of CH_4 occur below the aircraft and the CO_2 concentration is constant – can be calculated from:

$$\mathrm{CSF} = 1.0 + (\mathrm{PSF} - 1.0) \cdot c \quad (1)$$

The conversion factor c depends on geometry (aircraft altitude, solar zenith angle), atmospheric distribution of the according trace gas, and the surface albedo/SSR.

Assuming an average mixing ratio of 1774 ppb for CH_4, the concentration change in the total column below the aircraft ΔC is then estimated by the following equation:

$$\Delta C_{\mathrm{ppb}} = (1774\ \mathrm{ppb} \cdot \mathrm{CSF}) - 1774\ \mathrm{ppb} \quad (2)$$

Currently the WFMD/M retrieval algorithm is modified to invert directly changes below the aircraft. MAMAP zenith sky data are used to compare to nadir data, to derive column changes and to validate the assumption of an unchanged column above the aircraft.

AMTD
3, 3199–3276, 2010

4 Performance assessment of the SWIR channel

The instrument performance of the SWIR channel of MAMAP has been evaluated in two different ways: (i) by estimation of the signal-to-noise ratio (SNR) for each measured spectrum (Sect. 4.1) and (ii) by estimation of the instrument precision (Sect. 4.2). Time series of single detector readout and co-added burst mode measurements obtained for different operation conditions (on ground and in-flight) are analysed and compared in Sect. 4.3. In Sect. 4.4 the spectral stability of the system is examined. The on-ground measurements were carried out in May 2006 on the campus of the University of Bremen. The in-flight measurements were performed onboard the AWI Polar-5 aircraft and the FU-Berlin Cessna 207 aircraft during campaigns in August 2007 and November 2008. In the following sections the terms precision, accuracy and measurement uncertainty are used. These are defined as follows:

- precision includes all random errors in the measurement and the retrieval resulting from detector shot noise, random illumination effects and other random effects. As systematic fast varying (near random) albedo/SSR effects can not be separated from the other fast random effects, they also are accounted for in the precision.
- accuracy includes all systematic errors in the measurement and the retrieval resulting from aerosols and clouds, (constant) uncertainties in the slit function shape, errors resulting from the a-priori profile and temperature information, the spectroscopic line parameters, SZA effects, the flight altitude and other systematic errors.
- measurement uncertainty is defined as the sum of both, systematic and random errors.

4.1 Signal to noise ratios (SNRs)

The SNR of MAMAP determines (in combination with spectral resolution and spectral sampling) to a large degree the achievable precisions with these type of spectrometers.

AMTD
3, 3199–3276, 2010

The SNR for the SWIR band of MAMAP was evaluated in two different ways: (i) by an estimate via simulations (Sect. 4.1.1) and (ii) by a SNR estimate from real measurements (Sect. 4.1.2). Results for both estimates are later compared and discussed in Sect. 4.3 for different operation conditions.

4.1.1 SNR computations based on simulations

A theoretical noise (N) estimate for single detector readouts of the MAMAP system was inferred by applying the MAMAP instrument model simulation to a radiative transfer model spectrum. The noise for each detector pixel was calculated from the resulting shot noise of the estimated detector signal, the shot noise of the detector dark signal, the readout noise of the detector and the analog to digital converter. The simulated SNR for each detector pixel (SNR(sim)) was calculated by dividing the calculated detector signal (S) by the calculated noise (N).

$$\mathrm{SNR(sim)} = S/N \tag{3}$$

To simulate the functioning of MAMAP, a model was developed, based on the CarbonSat instrument model (Bovensmann et al., 2010), which is similar in concept to that used for SCIAMACHY. For comparison, simulated signals (in [BU]) and simulated SNR values (SNR(sim)) for different operation conditions are averaged over all detector pixels of the entire fitting windows of CH_4 and CO_2, and summarized in Table 4. In nominal operation, the MAMAP instrument utilises the so called "co-added burst mode". In this mode the instrument acquires a burst of a programmable number of n single spectra (typically n=10). All acquired spectra of each burst are co-added during subsequent processing (Sect. 2). Assuming a Gaussian error distribution for the single detector readouts, the simulated co-added burst mode (BM) signal-to-noise ratio ($\mathrm{SNR_{BM}(sim)}$) of each co-added measurement was calculated from the simulated single readout SNR(sim) by:

$$\mathrm{SNR_{BM}(sim)} = \mathrm{SNR(sim)} \cdot \sqrt{n} \tag{4}$$

AMTD
3, 3199–3276, 2010

4.1.2 SNR estimates from real data

For comparison with the modelled values, the SNR of MAMAP was estimated from real data. The SNR has been calculated from the individual fit residuum ("RES_i", see Sect. 3) of each single measurement for the two fit-windows used for CH_4 and CO_2. As RES_i of each ith measurement contains systematic features, the mean residuum for all measured spectra of the processed data set has been calculated and subtracted from the individual RES_i spectra to remove the systematic components contained in RES_i:

$$RES'_i = RES_i - \overline{RES}_{1\ldots n} \quad (5)$$

After subtraction RES'_i contains shot noise, detector noise, noise effects resulting from varying spectral structures of the measured (spectral) radiance, noise effects due to tilted illumination of the detector and noise effects resulting from inhomogeneous illumination. The latter result from changes of the instrument slit function, induced by keystone and smile effects of the optical system of the MAMAP spectrometer in combination with inhomogeneous illumination of the slit. Even-odd effects are induced by tilted illumination of the linear InGaAs detector.

To estimate the SNR of each measurement, first the standard deviation (SRES) of the resulting new fit residuals (RES'_i) has been retrieved for each single spectra:

$$SRES_i = SDEV(RES'_i) \quad (6)$$

The SNR of each measurement was then estimated by the reciprocal value of the standard deviation:

$$SNR(ret)_i = 1/SRES_i \quad (7)$$

For comparison with the simulated values, also the mean SNR values $\overline{SNR}(ret)_{1\ldots n}$ and mean measured signal values $\overline{S}(meas)$ were calculated for a selected set of measurement sequences and summarized in Table 4 (see Sect. 4.3). For co-added burst-mode

AMTD
3, 3199–3276, 2010

(see Sect. 4.1.1) the retrieved SNR (SNR_{BM}(ret)) has been estimated in a similar way as for the single detector readouts but using the burst averaged residua. The results are summarized in Table 6.

4.2 CO_2 and CH_4 retrieval precisions

The instrument precision which can be reached by a grating spectrometer system can be theoretically evaluated as performed in Sect. 4.2.1 or retrieved from real data sets as performed in Sect. 4.2.2. Results for both estimates are compared for different operation conditions in Sect. 4.3.

4.2.1 Theoretical retrieval precisions

The theoretical retrieval precision of MAMAP for CH_4 and CO_2 was estimated from the corresponding simulated SNR (Sect. 4.1.1) and from the instruments spectral resolution and spectral sampling. The solution of the WFMD/M algorithm is based on a least squares approach of the following form:

$$\boldsymbol{y} = \mathbf{K} \cdot \boldsymbol{x} + \boldsymbol{\epsilon} \tag{8}$$

where $\mathbf{K}$ denotes the weighting function matrix, $\boldsymbol{y}$ denotes the wavelength dependent difference between measurements and model, and $\boldsymbol{x}$ the parameters to be retrieved. The error is expressed by $\boldsymbol{\epsilon}$. With the inverse measurement covariance matrix $\mathbf{C}_y^{-1}$ derived for the simulated SNR the weighted least squares solution can be written as:

$$\boldsymbol{x} = (\mathbf{K}^t \mathbf{C}_y^{-1} \mathbf{K})^{-1} \mathbf{K}^t \mathbf{C}_y^{-1} \boldsymbol{y} \tag{9}$$

with the corresponding parameter covariance matrix:

$$\mathbf{C}_x = (\mathbf{K}^t \mathbf{C}_y^{-1} \mathbf{K})^{-1} \tag{10}$$

The diagonals give the variance of the parameters. Hence the simulated profile scaling factor precision PSFP can be calculated (for 1 σ) as:

$$\mathrm{PSFP(sim)}_{CH_4} = \sqrt{C_{x,CH_4}} \qquad \text{for } CH_4 \tag{11}$$

AMTD
3, 3199–3276, 2010

and

$$\mathrm{PSFP(sim)}_{\mathrm{CO_2}} = \sqrt{C_{x,\mathrm{CO_2}}} \qquad \text{for } \mathrm{CO_2}. \tag{12}$$

Results for the individual PSFP(sim) calculated for different instrument operation conditions are summarized in Table 4. Accordingly, the simulated precision for the profile scaling factor ratios PSFRP(sim) was calculated from the square root of the individual simulated PSF precisions ($\mathrm{PSFP}_{\mathrm{CH_4}}$(sim) and $\mathrm{PSFP}_{\mathrm{CO_2}}$(sim)) of each gas:

$$\mathrm{PSFRP(sim)} = \sqrt{\mathrm{PSFP}_{\mathrm{CH_4}}(\mathrm{sim})^2 + \mathrm{PSFP}_{\mathrm{CO_2}}(\mathrm{sim})^2} \tag{13}$$

Assuming a Gaussian error distribution for the single measurements obtained by MAMAP, the simulated co-added burst mode (BM) PSFR precision ($\mathrm{PSFRP}_{\mathrm{BM}}$(sim)) of each co-added measurement can be calculated from the simulated single readout PSFR precisions (PSFRP(sim)) and the number of co-added measurements as:

$$\mathrm{PSFRP}_{\mathrm{BM}}(\mathrm{sim}) = \mathrm{PSFRP(sim)} \;/\; \sqrt{n} \tag{14}$$

4.2.2 Precision estimates obtained using real data

To estimate the instrument precision for a given data set, the individual $\mathrm{CH_4}$ and $\mathrm{CO_2}$ columns were processed for each single measured spectra with the WFMD/M retrieval algorithm as described in Sect. 3. To account for small systematic offsets caused by the fit procedure, each series of profile scaling factors (PSF_i) was first normalized for each gas by the mean value of all measurements of the processed data set. The resulting normalized profile scaling factors NPSF_i can be calculated as:

$$\mathrm{NPSF}_i = \mathrm{PSF}_i / \overline{\mathrm{PSF}}_{1\ldots n} \tag{15}$$

To account for path differences caused by topography and movements of the plane the (normalized) $\mathrm{CH_4}/\mathrm{CO_2}$ profile scaling factor ratio (PSFR_i) was calculated as discussed in Sect. 3:

$$\mathrm{PSFR}(\mathrm{CH_4}/\mathrm{CO_2})_i = \mathrm{NPSF}(\mathrm{CH_4})_i / \mathrm{NPSF}(\mathrm{CO_2})_i \tag{16}$$

AMTD
3, 3199–3276, 2010

To account for slow SZA and atmospheric variations the CH_4/CO_2 PSFR were additionally high-pass filtered. The retrieved profile scaling factor ratio precision PSFRP(ret) was then calculated as standard deviation of the $PSFR_i$ over the whole investigated data set:

$$\mathrm{PSFRP(ret)} = \mathrm{SDEV}\left(\mathrm{PSFR}(CH_4/CO_2)_{1\ldots n}\right) \quad (17)$$

This procedure was repeated for a set of measurement sequences for different operation conditions of the instrument as described in the next section. The obtained results from these sequences are summarized in Table 4 and compared to simulated values (see Sect. 4.2.1). For co-added burst-mode (see Sect. 4.1.1) the retrieved profile scaling factor ratio precision $PSFRP_{BM}$(ret) has been estimated in a similar way as for the single detector readouts, but using the burst averaged profile scaling factors PSF_{BM} instead. Results for co-added burst mode obtained from one data set are summarized in Table 6.

4.3 Single exposure SNR and precision for different operation conditions

To estimate the SNR and the PSFR precision (PSFRP) of the MAMAP instrument under different operating conditions, a data set of seven measurement sequences has been selected, including static on-ground and dynamic in-flight measurements. The in-flight sequences have been subdivided into measurement sequences over surfaces containing primarily homogeneous and surfaces containing primarily inhomogeneous distribution of the measured radiance (see Table 3). These sequences produce primarily homogeneous and variable inhomogeneous illumination conditions on the spectrometers slit, respectively. In addition, sequences of zenith sky in-flight measurements were investigated for which the slit was illuminated uniformly. In the following results obtained for the different operation conditions will be presented and discussed. For all sequences CH_4 and CO_2 $\overline{\mathrm{SNR}}$ values, profile scaling factors (PSF) and associated PSFR precisions have been retrieved for single detector readouts as described in

AMTD
3, 3199–3276, 2010

Sect. 4.2. For comparison also the associated simulated $\overline{\mathrm{SNR}}$ values and PSFR precisions were computed as described in Sects. 4.1 and 4.2. All results of these calculations are summarized in Table 4. By inter-comparison of the different results, potential error sources affecting the instrument performance can be identified or excluded.

4.3.1 Ground based measurements

To investigate the instrument's performance under vibration-free static conditions, two types of on-ground measurements have been performed. In a first set-up the nadir telescopes of the spectrometer have been pointed towards a group of trees. This configuration is referred to as "pseudo" nadir or "sun-illuminated target" (SIT) configuration. The trees were located on the campus of the University of Bremen, in approximately 250 m distance to the MAMAP spectrometer. In this configuration a measurement sequence was acquired with a single readout exposure time of 148 ms at ~70% detector saturation. The illumination conditions (signal levels) were nearly constant due to (nearly) clear sky conditions, in contrast to typical in-flight conditions, where the signal varies as a result of changes in the surface albedo/SSR.

In a second on-ground set-up, scattered light zenith radiance measurements (measurements of the down-welling diffuse radiance) were performed by pointing the MAMAP zenith telescopes directly into the sky. The single readout exposure time for the acquired sequence was 700 ms at ~56% detector saturation and clear sky conditions.

The measurements have not been absolutely calibrated but have been corrected for dead and bad pixels and dark signal. The spectra were also normalized using a white light source (WLS) spectrum to account for pixel to pixel gain variations and etalons. The spectrometers were temperature stabilized being heated to ~26 °C for an outside temperature of ~15–20 °C.

After processing of both measurement sequences a RMS of the fit residuum (Sect. 3) in the range of 0.5–0.6% was achieved (i.e. very similar to the RMS obtained for well

AMTD
3, 3199–3276, 2010

filtered in-fight measurements, see Fig. 5).

Figure 8 shows precision and RMS results obtained for the on-ground sequences after processing. On the left, the results from the sun illuminated target (SIT) measurements performed on 11 May 2006 are displayed. On the right, the results from ground-based scattered zenith radiance measurements performed on 10 May 2006 are shown. The top panel shows the normalized PSFR precisions for CH_4/CO_2. The second panel shows the measured signal in [BU] (for 16 bit ADC) with dark signal subtracted. The bottom panel shows the SNR estimate of each measurement for each gas (CH_4 black, CO_2 red symbols) as described in Sect. 4.1.2.

It is assumed that the precision and the SNR of the MAMAP instrument under static conditions on ground is primarily dominated by the shot noise of the measured signal, the dark signal shot noise and readout noise of the detector and front-end electronics. Vibrations or changes in the illumination conditions of the spectrometers can be omitted. Therefore good agreement between measurements and model simulations is expected.

For the SIT measurements (as expected) a very good agreement between simulated and retrieved SNR values can be achieved for single detector readouts. The simulated $\overline{\text{SNR}}$(sim) values for CH_4 and CO_2 are 1584 and 1605 vs. the retrieved $\overline{\text{SNR}}$(ret) values of 1566 and 1651. The respective CH_4/CO_2 simulated vs. retrieved PSFR precision for 148 ms exposure time was 0.27% (PSFRP(sim)) vs. 0.33% (PSFRP(ret)). Thus also for the precision, good agreement between model simulations and measurements can be obtained (Table 4).

For the scattered zenith sky radiance measurements, the mean SNR is in good agreement ($\overline{\text{SNR}}$(sim)=1319 vs. $\overline{\text{SNR}}$(ret)=1181 for CH_4 and $\overline{\text{SNR}}$(sim)=1338 vs. $\overline{\text{SNR}}$(ret)=1290, respectively for CO_2). In contrast, the simulated and retrieved CH_4/CO_2 PSFR precisions deviate by a factor of two (0.33% (PSFRP(sim)) vs. 0.63% (PSFRP(ret)), for 700 ms exposure time). The origin of this difference is not yet identified. It may possibly be induced by atmospheric variations caused by turbulences and light path differences caused by aerosol scattering inside the measured air masses.

AMTD
3, 3199–3276, 2010

Another possibility is absorption of liquid water or ice in aerosol and cirrus clouds, which results in a broad band absorption at the short wavelength end of the channel but is not explicitly accounted for in the retrieval. In general measurements in scattered zenith sky radiance geometry are likely to be more affected by atmospheric variations than measurements in SIT ("pseudo" nadir) geometry where the solar radiation is scattered/reflected primarily by the target opposed to the atmosphere.

Figure 7 shows a time series of SIT measurements under slightly variable atmospheric conditions. On the left results from single readout processing are shown. The top panel shows PSFs obtained for both gases (CH_4 black, CO_2 red symbols). The second panel shows the CH_4/CO_2 PSFR. The bottom panel shows the measured signal in [BU] with dark signal subtracted. On the right, in analogy to the nominal in-flight burst mode (Sect. 4.3.4) results for the same time series with 10 co-added readouts are displayed. For the latter, the simulated burst mode PSFR precision ($PSFRP_{BM}$ (sim)) can be calculated from the single readout precision as (see Sect. 4.2.1):

$$PSFRP_{BM}(sim) = 0.27/\sqrt{10} = 0.0854\% \quad (18)$$

Comparison with the second panel on the right shows reasonable agreement of the $PSFRP_{BM}$(sim) with the measured values. The systematic impact of atmospheric variability on the CH_4 and CO_2 PSF accuracy variation is attributed to thin clouds. This exceeds the precision of the single measured values. Improving the retrieval to identify and account explicitly for thin cloud effects will further improve the accuracy of the retrieval.

4.3.2 Airborne single readout measurements over homogeneous scenes

To investigate the instrument performance under airborne conditions, the spectrometer rack (containing the SWIR and NIR spectrometer systems) was attached with 6 anti-vibration mounts to an aluminium aperture plate. This aperture plate contains two 10 mm thick wedged Suprasil aperture windows with a diameter of 180 mm. The aperture plate itself was directly attached with screws to the structure of the plane (Fig. 4).

AMTD
3, 3199–3276, 2010

Apart from vibrations, etalons from the Suprasil aperture windows and the spectrometer itself, spectral shifts caused by thermal gradients inside the spectrometers optical bench and effects from inhomogeneous slit illumination influence the in-flight measurements. To separate instrumental and vibration effects from illumination effects, first nadir measurement sequences over water and land with nearly homogeneous distribution of the measured radiance were investigated. It is thereby assumed that measurement sequences with smaller variations of the measured radiance (i.e. detector filling) will produce more homogeneous slit illumination conditions than measurement sequences where strong variations occur. To avoid detector saturation during airborne operation, the detector is operated in nadir mode typically at ~10–20% of the total full well capacity (~6000–13 000 [BU] at 16 bit resolution) corresponding to surface albedo/SSR over land in the range between 0.10–0.20. The exposure time of each readout for these albedos/SSRs over land was typically in the range of 60–100 ms, depending on solar zenith angle. Respectively over water (with typical albedos/SSRs of ~0.01) exposure times in the range between 0.6 s and 1 s were applied.

In Fig. 9 and Fig. 10 same plots as for ground based measurements (Fig. 8) are shown, but for dynamic in-flight conditions in nadir observation mode. The nadir measurement series over water are taken over the Caribbean Sea (9 Novomber 2008). The nadir measurement series over land are taken within the United States (7 November 2008). Both measurements are performed on board the AWI Polar-5 aircraft. On the left side of both figures (Fig. 9 and 10) measurement sequences for homogeneous and on the right side measurement sequences for inhomogeneous surface radiance distributions are presented.

Beside nadir measurements also airborne zenith irradiance measurement sequences were investigated. For this the instrument observes the upper hemispheric downwelling radiance and solar irradiance through a set of 4 transmissive Spectralon diffuser plates. The incoming radiation is fed from the diffusers to the instrument via glass fibers. Two lenses are imaging the fibers via the zenith optical path (Fig. 1) directly onto the slit of the spectrometer. In this mode of operation, the slit is always

AMTD
3, 3199–3276, 2010

homogeneously illuminated and no additional spectral structures (as for instance due to features in the SSR) exist.

On the left, Fig. 11 shows measurement sequences taken by the zenith optical path of the instrument. The measurement is performed on board of a Cessna-207 aircraft. The readout to readout variation of the measured irradiance is very similar to that observed on ground (i.e. SIT measurements, Fig. 8).

The airborne zenith irradiance measurements (ZIR) show good agreement between simulated and retrieved SNR values ($\overline{\text{SNR}}$(sim)=611 vs. $\overline{\text{SNR}}$(ret)=570 for CH_4 and $\overline{\text{SNR}}$(sim)=621 vs. $\overline{\text{SNR}}$(ret)=620, respectively for CO_2). The according simulated vs. retrieved PSFR precisions for single detector readouts and 400 ms exposure time were 0.72% (simulated) vs. 0.59% (retrieved).

For homogeneous radiance over water (WHO) also reasonable agreement between simulated and retrieved SNR and precisions are achieved ($\overline{\text{SNR}}$(sim)=533 vs. $\overline{\text{SNR}}$(ret)=422 for CH_4 and $\overline{\text{SNR}}$(sim)=542 (CO_2) vs. $\overline{\text{SNR}}$(meas)=411 for CO_2). For single detector readouts and 1 s exposure time the respective simulated vs. retrieved PSFR precisions were 0.83% (simulated) vs. 1.12% (retrieved).

Over land targets with homogeneous upwelling radiance (LHO) the simulated vs. measured SNR were also in good agreement ($\overline{\text{SNR}}$(sim)=628 (CH_4) vs. $\overline{\text{SNR}}$(ret)=538 for CH_4 and $\overline{\text{SNR}}$(sim)=638 vs. $\overline{\text{SNR}}$(ret)=588 for CO_2). The respective simulated vs. retrieved PSFR precisions for single detector readouts and 58 ms exposure time were 0.71% (simulated) vs. 1.10% (retrieved) and agree also reasonably.

From these results it can be concluded that the in-flight measurements were barely affected by vibration effects or fast changing etalons. Assuming concentration changes to only occur in the CH_4 column below the aircraft and the CO_2 column as constant, the total column precision for CH_4 ($CP_{\%}(CH_4)$) can be estimated from the PSFR precision and the conversion factor c for CH_4 (see Sect. 3) as:

$$CP_{\%}(CH_4) \approx \text{PSFRP} \cdot c(CH_4) \quad (19)$$

AMTD
3, 3199–3276, 2010

For an aircraft altitude of 4500 m, SZA of 40° and an albedo/SSR of 0.01 the CH_4 single readout column precision $CP_{\%}(CH_4)$ for measurements over water with homogeneous radiance (WHO) can be estimated to ~0.94% (for exposure time=1 s). For the same plane altitude and SZA the single readout CH_4 column precision over land surfaces with homogeneous radiance (LHO) can be estimated to ~0.75% (for exposure time=58 ms).

4.3.3 Airborne single readout measurements over inhomogeneous scenes

To investigate effects of inhomogeneous illumination of the slit, airborne nadir measurement time series taken over water and land surfaces with inhomogeneous upwelling radiance were analyzed. The simulated and retrieved mean SNR values over water with inhomogeneous radiance deviate approximately by a factor of two ($\overline{SNR}$(sim)=1047 vs. $\overline{SNR}$(ret)=532 for CH_4 and $\overline{SNR}$(sim)=1063 vs. $\overline{SNR}$(ret)=598 for CO_2). The according PSFR precisions were 0.42% (simulated) vs. 2.74% (retrieved) and deviate by a factor of ~6.5.

For land surfaces with inhomogeneous radiance similar results are obtained. The obtained simulated and retrieved mean SNR values were $\overline{SNR}$(sim)=628 vs. $\overline{SNR}$(ret)=418 for CH_4 and $\overline{SNR}$(sim)=638 vs. $\overline{SNR}$(meas)=475 for CO_2. The according PSFR precisions were 0.71% (simulated) vs. 2.8% (retrieved) and deviate by a factor ~3.9.

The degraded performance under inhomogeneous illumination conditions is attributed primarily to smile and keystone effects of the spectrometer system's optical bench, combined with an inhomogeneous illumination of the slit. This assumption is supported by ZEMAX® optical design program end to end simulations of the optical system of MAMAP, showing that inhomogeneous slit illumination leads to variations of the slit function shape and position. Such variations induce errors in the retrieval. Other factors like even-odd effects of the used linear InGaAs detector also caused by inhomogeneous illumination (i.e. even-odd effects due to tilted detector illumination)

AMTD
3, 3199–3276, 2010

can be accounted for by the WFMD/M algorithm and are believed to play a minor role. Effects such as small spectral features of the earthshine spectral reflectance can also not be completely excluded as reason. All single readout time series results obtained for the different operation conditions are summarized in Table 4.

To minimize effects of inhomogeneous illumination of the slit, a modification of MAMAP's optical bench has been initiated. After this modification it is expected that the instrument will reach the same or similar performances as over surfaces with homogeneous radiance distribution.

Assuming concentration changes to only occur in the CH_4 column below the aircraft and the CO_2 column as constant, the CH_4 single readout total column precision for a plane altitude of 4500 m, SZA of 40°, albedo/SSR of 0.01 and exposure time of 1 s can be estimated to be ~2.30% (see Table 2 for conversion factors) for water with inhomogeneous radiance (WIH). For the same plane altitude and SZA the single readout CH_4 column precision over land surfaces with inhomogeneous radiance (LIH) can be estimated to be ~1.87% of the total column (for exposure time = 58 ms and albedo/SSR ~0.18).

4.3.4 MAMAP nominal co-added burst mode

In this section, the MAMAP precision for the nominal burst mode of operation over land targets will be discussed. Over land targets typically bursts of 10 measurements were acquired and co-added to one measurement (see Sect. 2.1) to reach an appropriate SNR (i.e. SNR≈1000). The retrieved burst mode SNR (SNR_{BM}(ret)) and burst mode PSFR precision ($PSFRP_{BM}$) have been estimated in a similar way as for the single detector readouts (see Sects. 4.2 and 4.3), using the burst averaged residua and PSFR values, respectively.

The simulated and retrieved burst mode mean SNR values and PSFR precisions are summarized in Table 6. These were calculated for the same measurement series over land surfaces with inhomogeneous radiance (LIH) as described for single readouts in Sect. 4.3.3. In this section, only the worst case scenario (i.e. precision over surfaces

AMTD
3, 3199–3276, 2010

with inhomogeneous radiance distribution) is investigated.

For integration times (=exposure time · number of co-added spectra) of ~580 ms the mean simulated vs. estimated $\overline{SNR_{BM}}$ values for measurements over surfaces with inhomogeneous radiance were $\overline{SNR_{BM}}(sim)=1986$ (CH_4) and $\overline{SNR_{BM}}(sim)=2017$ (CO_2) vs. $\overline{SNR_{BM}}(ret)=827$ (CH_4) and $\overline{SNR_{BM}}(ret)=957$ (CO_2). The respective simulated vs. retrieved burst mode PSFR precisions were $PSFRP_{BM}(sim)=0.225\%$ vs. $PSFRP_{BM}(ret)=1.74\%$. It is obvious that the retrieved burst mode precision is about a factor ~7.7 lower compared to the simulated values.

Assuming a Gaussian error distribution for the measurements, the burst mode PSFR precision and burst mode SNR can be derived for inhomogeneous targets (LIH) also in a indirect way. This was done by multiplication (i.e. for SNR calculation) or division (i.e. for precision calculation) of the retrieved single readout SNR ($\overline{SNR_{SR}}(ret)$) and single readout precision values ($PSFRP_{SR}(ret)$) (Sect. 4.3.3) with the square root of 10 (for n=10 measurements per burst).

The resulting indirectly derived mean burst mode SNR ($\overline{SNR_{BM}}(ret)'$) was $\overline{SNR_{BM}}(ret)'=418\cdot\sqrt{10}=1322$ for CH_4 and $\overline{SNR_{BM}}(ret)=475\cdot\sqrt{10}=1502$ for CO_2. The according indirectly derived precision ($PSFRP_{BM}(sim)'$) was $PSFRP_{BM}(sim)'=2.8\%/\sqrt{10}=0.89\%$.

From the comparison of both directly derived and indirectly calculated SNR values and PSFR precisions ($\overline{SNR_{BM}}(ret)$ vs. $\overline{SNR_{BM}}(ret)'$ and $PSFRP_{BM}(ret)$ vs. $PSFRP_{BM}(meas)'$) with the simulated values it is evident that random Gaussian error distribution can not be assumed for the single measured spectra.

This result supports the attribution of the random PSF errors observed with MAMAP to the inhomogeneous illumination of the spectrometer's slit and the variations in slit function position and shape, caused by keystone and smile effects. Ground structures like edges parallel to the flight direction can produce similar deviations in all 10 measurements of one burst. Therefore random Gaussian error distribution can not be assumed. Spectral features in the earthshine spectral reflectance cannot be completely

AMTD
3, 3199–3276, 2010

excluded either. In contrast, it is assumed that shot noise and noise of the readout electronics and the detector should produce random Gaussian error distributions like demonstrated for ground based measurements.

From these findings it can also be expected that the undergoing modification of the optical bench of the MAMAP instrument for reducing inhomogeneous slit illumination effects can lead to a significant improvement of the instrument's burst mode SNR and precision characteristics. Assuming that the instrument can then reach SNR and precision values similar to those achieved for single readouts over homogeneous land targets (LHO, Table 4), it can be estimated for burst mode, that SNR values in the order of $\overline{\mathrm{SNR}}_{\mathrm{BM}}(\mathrm{meas})' = 538 \cdot \sqrt{10} = 1713$ for CH_4 and $\overline{\mathrm{SNR}}_{\mathrm{BM}}(\mathrm{meas})' = 588 \cdot \sqrt{10} = 1859$ for CO_2 remain feasible. The according feasible burst mode PSFR precision may reach a factor of ~5 better values than actually achieved (i.e. up to $\mathrm{PSFRP}_{\mathrm{BM}}(\mathrm{ret})' = 1.10\% / \sqrt{10} = 0.35\%$).

Assuming again concentration changes to only occur in the CH_4 column below the aircraft (and the CO_2 column as constant), the actual MAMAP CH_4 co-added burst mode total column precision ($\mathrm{CP}_{\mathrm{BM},\%}$) over inhomogeneous land surfaces (LIH) can be estimated from the PSFR precision of ~1.74% to be ~1.16% (1 σ) for a plane altitude of 4500 m, integration times of 580 ms, SZA of 40° and an albedo/SSR of 0.18. For a background concentration 1774 ppb this corresponds to an enhancement oft 20.59 ppb of the total column.

By calculating the equivalent total column light path L_e through the atmosphere as $L_e = g/(\rho g) \approx 8576\,\mathrm{m}$ (for $p = 1013\,\mathrm{hPa}$, $\rho = 1.2041\,\mathrm{kg/m^3}$, $g = 9.81\,\mathrm{m/s^2}$) the total column precision of MAMAP is converted to ppm m for comparison with other instruments (SZA 40°, albedo/SSR 0.18):

$$\mathrm{CP}(\mathrm{CH_4})_{\mathrm{ppm\ m}} \approx 20.59\ \mathrm{ppb} \cdot 8576\,\mathrm{m} = 177\,\mathrm{ppm\ m} \quad (20)$$

For a typical SZA of 40° the estimated column precision of 177 ppm m is inside the instrument threshold requirement, which is to measure the total column concentration in nadir with a precision of 1–2% with respect to the atmospheric background,

AMTD
3, 3199–3276, 2010

corresponding to a precision of ~150–300 ppm m. For a lower plane altitude of 850 m the 1 σ precision becomes 142 ppm m.

After the planned modification of the instruments optical bench to account for inhomogeneous slit illumination, a precision of the total column for a plane altitude of 850 m and integration time t_{int}=600 ms of approximately

$$\begin{aligned} CP(CH_4)_{ppm\ m} &\approx 1774\ ppb \cdot 0.0035 \cdot c(CH_4) \\ &= 4.22\ ppb \quad (\approx 33\ ppm\ m) \end{aligned} \tag{21}$$

is predicted.

In that case the MAMAP CH_4 total column uncertainty variation will not be limited by the precision of the instrument. Below 1% total column precision, the accuracy variation induced by atmospheric effects (i.e. light path differences for CH_4 and CO_2 caused by scattering and absorption of aerosols and clouds and variations of the albedo/SSR and refractive index of the atmosphere) start to dominate the overall uncertainty variation.

4.4 Spectral stability

To investigate further the attribution of the degradation of the precision of MAMAP data products between inhomogeneous and homogeneous ground scenes to the inhomogeneous slit illumination and related model simulations, the short term spectral shifts in the observations over surfaces having respectively homogeneous and inhomogeneous radiance were analysed. It is assumed that any impact of the aircraft vibration for the different measurement series are similar. A comparison of short term spectral shifts derived by non-linear least squares fitting for inhomogeneous and homogeneous water surfaces shows a change of up to a factor of two: spectral shifts being 0.0049 nm for homogeneous scenes as compared to 0.0101 nm for inhomogeneous scenes above water. For land surfaces a similar deviation was observed: the spectral shift being 0.0180 nm for homogeneous compared to 0.0364 nm for inhomogeneous land surfaces. The different exposure times of 1 s over water and 58 ms over land and

AMTD
3, 3199–3276, 2010

the difference in inhomogeneity distribution between land and water surfaces are attributed to the differences in the observed shifts. Thus the factor of two decrease in spectral stability in both cases (for land and for water) is consistent with a degraded performance of MAMAP being explained by inhomogeneous illumination effects of the spectrometers slit. For comparison, additionally to the airborne nadir measurements spectral shift results from ground based radiance and airborne zenith sky irradiance measurements are summarized in Table 5. MAMAP achieves for the fastest exposure times over homogeneous land targets (LHO), where the spectral shifts are expected to be dominated primarily by vibrations, a spectral stability of ~1/46 of the FWHM of 0.82 nm (i.e. close to the required value of 1/60 of the FWHM).

5 MAMAP targets

Achieving 1–2% total column accuracy for the data products $X\mathrm{CH_4}$ and $X\mathrm{CO_2}$ from a single ground scene measurement (corresponding to 150–300 ppm m ($1\,\sigma$) column change for $\mathrm{CH_4}$ below the aircraft (see Sect. 4)), is challenging for an airborne and spaceborne passive remote sensing instrument (Bréon and Ciais, 2010). Nevertheless, such a performance puts limitations on the target emissions which are suitable to be detected with the actual MAMAP total column precision of 1%. Because of the large background concentrations of $\mathrm{CH_4}$ and $\mathrm{CO_2}$, an emission source must have an appropriate emission strength and horizontal extent in order to build up a column enhancement which can be detected.

In the following we discuss the conditions under which MAMAP can obtain information about supposed target emissions. For this purpose we use a simple model to relate the surface flux F of a given gas to the relative change of its vertical column $\Delta V/V$ over a distance l along the main wind direction. In this section two cases are considered: (i) a range of targets from a well isolated source region of the size of a MAMAP footprint up to an area, observed by MAMAP in several minutes i.e. ~25 m up to a few 10 km. Possible targets are landfills, seeps, fugitive emissions of gas/oil industry, power plants,

AMTD
3, 3199–3276, 2010

steelworks, coal mines and (mud) volcanoes, (ii) an effectively homogeneous source region with an extension larger than ~50 km such as extended wetlands.

For an isolated source region, time independent (static) meteorological conditions can be assumed as a first approximation for short periods of time where measurements are taken over and near the source. These conditions are characterized by clear sky over the measurement area, small atmospheric variations of the cloud and aerosol optical thickness, small solar zenith angle variations and constant wind speeds. For such conditions, systematic accuracy variations in the CH_4/CO_2 column caused by light path differences induced primarily by an inadequate modelling of the scattering of electromagnetic radiation by aerosols and optical thin cirrus clouds (Schneising et al., 2009; Schneising, 2009) is assumed to be negligible (Krings et al., manuscript in preparation). In addition assuming that aerosol and cloud are smoothly varying, any impact of slow systematic changes in the accuracy of the measured CH_4/CO_2 column mixing ratio can be minimised by high-pass filtering the data. Strong local sources produce short term or short duration concentration changes for the flight path as compared to any changes produced by the variation of aerosols and (thin) cirrus clouds. For such conditions the detection limit of MAMAP is primarily dominated by the instrument precision rather than by variation of the accuracy.

Assuming a constant wind speed u in the horizontal $+x$ direction in the layer of interest and a mean flux F as first approximation, the resulting enhancement ΔV of the vertical column V can be estimated as follows: $\Delta V = F \cdot t$, where t is the accumulation time, which characterizes the time available for an air column to accumulate when it moves over the target. For a target with extension l it follows $t = l/u$. The relative increase of the vertical column over the target is given by $\Delta V/V = F/V \cdot l/u$. The smallest detectable flux F_{min} for a given situation is then given by:

$$F_{\mathrm{min}} = \Delta V/V \cdot V \cdot u/l. \quad (22)$$

AMTD
3, 3199–3276, 2010

Assuming for the estimate a constant wind speed of u=2 m/s and all concentration changes to occur below the aircraft, a horizontal extent of the emission source of $l \approx 400$ m (e.g. a landfill) and the required total column enhancement $\Delta V/V$ equal to ~1% total column precision (~150 ppm m for CH_4 and 32 600 ppm m for CO_2) of MAMAP for inhomogeneous scenes. With a typical value for the CH_4 background column of V=10 g CH_4/m^2 ($3.6 \cdot 10^{19}$ molecules/cm^2) the smallest detectable flux F_{min} can then be calculated to be 1.8 g $CH_4/m^2/h$. At a constant wind speed of 2 m/s the product of flux F and source extension l is the main parameter which can be calculated for 1% enhancement to be $F_{min} \cdot l = 0.01 \cdot 10$ g $CH_4/m^2 \cdot 2$ m/s=0.2 g $CH_4/m/s$. Equivalent calculations can also be performed for CO_2.

Over the globe, many different sources exist with fluxes exceeding the above calculated detection limits. For instance CH_4 emissions of landfills with organic waste and temporal coverage, equipped with gas recovery can reach mean CH_4 fluxes in the order of 2–4 g $CH_4/m^2/h$ (Fellner et al., 2003; Börjesson et al., 2000), i.e., larger than the actual detection limit of MAMAP. Furthermore Judd (2004) report CH_4 fluxes between 148 and 445 g $CH_4/m^2/h$ for the Coal Oil Point (COP) seep measured with tents for an area of 1800 m^2 near Santa Barbara, California. Miscellaneous strong dry seeps and mud volcanoes exist also in other parts of the world for instance at the Black Sea shelve offshore Georgia (Judd, 2004), in eastern Azerbaijan (Etiope et al., 2004) and Indonesia (Chakraborty and Anggraini, 2009). Strong seepage can also occur over shallow or submerged gas hydrates in arctic regions (Shakhova et al., 2010; Bowen et al., 2008). Other localized sources like fugitive emissions as the result of oil and gas well exploration and utilization by oil and gas industry can produce atmospheric fluxes strong enough to be detected with MAMAP as well. Jagovkina et al. (2000, and references therein) estimated for an area of $\sim 1.8 \cdot 10^{10}$ m^2 near Yamal in Russia a mean flux of 1–2 g $CH_4/m^2/d$. The corresponding detection limit of MAMAP for such an area (e.g. extend of $l \approx 50$ km) can be calculated to be in the range of $F_{min} \approx 0.35$ g $CH_4/m^2/d$ which is well below the reported values. Similar estimates can be performed for refineries and gas processing plants with fugitive emissions in the range of ~140–300 kgCH_4/h

AMTD
3, 3199–3276, 2010

(Chambers and Strosher, 2006a,b). Emissions from oilsands tailings settling basins with flux estimates between 0.1–4.8 g $CH_4/m^2/h$ (Siddique et al., 2008) also outrun the smallest detectable fluxes. Beside CH_4 also volcanic CO_2 emission (Mörner and Etiope, 2002) clearly exceed the detection limit of MAMAP.

These estimates show that MAMAP has the potential to detect strong local CH_4 and CO_2 emissions and corresponding gradients as shown in the next section. Under certain circumstances (i.e. knowledge of wind) also corresponding fluxes can be estimated when appropriate patterns are flown as demonstrated in Krings at al. (manuscript in preparation). After finalizing the modification of the optical system of MAMAP, it can be expected that the smallest detectable flux limit F_{min} can be improved significantly. In addition appropriate flight strategies allowing further averaging of the observations can also improve the precision. Thus detection of weaker localized sources can be expected in the future.

Many important CH_4 sources emit significantly smaller fluxes of CH_4 compared to the values reported above (for localized sources). Siberian wetlands emit typically in the order of ~20 mg $CH_4/m^2/d$ on average (Sachs et al., 2008) to up to ~200 mg $CH_4/m^2/d$ for summer seasons (Bohn et al., 2007). The approach used above can also be applied to estimate the detection limits required for extended regions of less intense source emissions assuming that the region is sufficiently homogeneous. For a strong summer CH_4 flux of F=200 mg $CH_4/m^2/d$ for Western Siberian wetlands, a constant wind speed of u=2 m/s, and a minimum detectable column enhancement of $\Delta V/V$=1% (corresponding to 150 ppm m below the aircraft), a required accumulation distance of $l \approx 86$ km can be calculated. In order to estimate gradients typically a larger distance is required (i.e. min. 3 times of the accumulation distance, ~250 km). This simple method to estimate the range of expected CH_4 total column changes emanating from these type of sources requires sufficiently stable conditions during the period of the aircraft measurement. When this requirement is not fulfilled, more complex regional chemical transport modelling (Jagovkina et al., 2000, 2001) is needed. For extended sources the smallest detectable flux F_{min} is restricted primarily by accuracy variations (i.e. the relative

AMTD
3, 3199–3276, 2010

accuracy) and not by the precision of the instrument. A detailed discussion on the impact of aerosols and thin clouds on the accuracy of MAMAP data products is given in Krings et al. (2010).

6 First results from measurements over localized emissions sources

In order to test the MAMAP sensitivity to score emissions and validate the results obtained in Sect. 4.3.4 flights over localized targets have been performed in summer 2007. In the following, results from flights over a target with poorly known CH_4 emission rate (i.e. a landfill) and targets with well characterized CO_2 emission rates (i.e. two power plants) are presented.

The flights were performed with a Cessna 207 aircraft, operated by the Free University of Berlin. The flights over the well characterized CO_2 targets focused on the coal fired power plants Jänschwalde and Schwarze Pumpe (located near Berlin, Germany). In the following we present results obtained with the SWIR channel for nadir observations only. Zenith observations are to be included in the retrieval algorithm in a subsequent studies.

The measurements were analyzed with the WFMD/M retrieval algorithm (see Sect. 3) using radiative transfer simulations performed with the SCIATRAN radiative transfer model (Rozanov et al., 2005).

The conditions of flight were such that the aircraft flew at 850 m altitude performing direct nadir observations. By computing the CO_2/CH_4 ratio of the measured and retrieved profile scaling factors for the CO_2 sources (assuming that CH_4 is constant) and vice versa (CH_4/CO_2) for the CH_4 source (assuming that CO_2 is constant), any line-of-sight errors, induced by rolling of the aircraft and lack of knowledge of altitude/ground distance are neglected (see Sect. 3). Systematic effects in the measured columns caused by solar zenith angle changes and cirrus cloud variations are minimised by high-pass filtering the data (see previous section).

AMTD
3, 3199–3276, 2010

For the RTM simulation, temperature, pressure, and water vapour vertical profiles corresponding to the US Standard Atmosphere, a constant albedo/SSR of 0.18 and a solar zenith angle of 40° (as calculated for the time of the overfligts) have been used. Clear sky (cloud free) conditions have been assumed although some partial cirrus covers have been reported during the flights.

Figures 12 and 13 show retrieved and normalized CO_2/CH_4 PSF ratios of MAMAP measurements of the power plant overflights near Berlin performed on 26 July 2007.

The target shown in Fig. 12 was the power plant Jänschwalde, operated by Vattenfall. This coal-fired power plant emits approximately 24.9 Mt CO_2/yr (EPER, 2004). On 26 July 2007 the plant emitted 56.6 t CO_2/min (Vattenfall, internal comunication). We estimated (depending on wind speed) that this emission roughly corresponds to a CO_2 total column increase (which is about $8{\cdot}10^{21}$ molecules/cm^2 for a surface pressure of about 1000 hPa and a CO_2 mixing ratio of 380 ppm) of few percent over and near the power plant (see Bovensmann et al., 2010).

The flight pattern has been chosen such that the aircraft was crossing several times the plume. The wind direction, which was almost perpendicular to the flight track, was clearly visible by the small steam clouds over the cooling towers (see photo Fig. 12). As can be seen in Fig. 12, elevated atmospheric CO_2 originating from the power plant and transported in wind direction, can clearly be detected with MAMAP. The elevated CO_2 is readily observed in the small map (on the right) showing the CO_2 PSF retrieved by the WFMD/M algorithm. The CH_4 PSF (the small map below) does not show such a clear pattern. This is as expected as there are no known local strong sources of CH_4 near the power plant. Also as expected, the ratio of the CO_2 to CH_4 profile scaling factors produce a smoother pattern, as light path errors due to, e.g., not yet considered changes of the aircraft rolling and distance to ground, cancel to a large extent when the CO_2/CH_4 PSF ratio is computed. The approximately 3% enhancement in the CO_2/CH_4 PSF ratio over the power plant shown in Fig. 12 is attributed to elevated CO_2. Assuming the changes of CH_4 as small and CO_2 variations to occur only below the aircraft the total column increase ΔC_{TC} CO_2 is estimated from the 3% enhancement of the PSF

AMTD
3, 3199–3276, 2010

ratio by:

$$\Delta C_{\mathrm{TC}}(\mathrm{CO_2}) \approx 380\ \mathrm{ppm} \cdot 0.03 \cdot c(\mathrm{CO_2}) = 4.86\ \mathrm{ppm} \quad (23)$$

in agreement with the predicted values. These results show that MAMAP reaches the initial sensitivity requirements very well. For more details on power plant emission measurement with MAMAP see also Bovensmann et al. (2010), Krings et al. (2010).

Figure 13 shows similar results as Fig. 12 but for overflights at the power plant Schwarze Pumpe, which has an output of approximately 10.9 Mt CO_2/yr (EPER, 2004). On the 26 July 2007 Schwarze Pumpe had an output of 26 t CO_2/min as reported by Vattenfall. The wind speed during both over flights was in the range of ~2.5–5.0 m/s. The figure shows that enhanced CO_2 values can clearly be observed downwind of the source with MAMAP.

Figure 14 shows an overflight transect measured over the landfill Vorketzin on 26 July 2007. During the transect wind speed was measured nearby the landfill. The mean wind speed was estimated to be in the order of 3 m/s from south, south-south-west direction. The path length of the accumulation of the air-mass over the landfill body is estimated to about ~450 m.

The anomaly in the retrieved normalized CH_4/CO_2 PSF ratio during the transect was in the range of +1–2% (Fig. 14). With a SZA of ~40° and an aircraft altitude of ~850 m and the assumption that the observed anomaly (of 2%) is mainly due to the increase of the CH_4 concentration below the aircraft, the corresponding enhancement in total column (for albedo/SSR of ~0.18) can be estimated to:

$$\Delta T_{\mathrm{CT},\%}(\mathrm{CH_4}) \approx 0.02 \cdot c(\mathrm{CH_4}) = 0.0112 \approx 1.12\% \quad \text{total column increase} \quad (24)$$

Assuming movement of the air-mass with constant speed (3 m/s) over the landfill body and that the adjacent wet-lands produce much less CH_4 (typically <60 mg CH_4/m^2/d) than the landfill body itself, the CH_4 total column increase of ~0.56–1.12% (after 450 m) leads to a rough estimate of the mean emission rate for the upper

AMTD
3, 3199–3276, 2010

central land fill area within ~1.24–2.48 g $CH_4/m^2/h$ or larger. For similar types of landfills (with organic waste, equipped with temporal covers and gas recovery systems) mean flux rates to the atmosphere in the order of 2–4 g $CH_4/m^2/h$ are reported (Fellner et al., 2003; Börjesson et al., 2000) as discussed in the previous section.

To exclude albedo/SSR dependent offsets as origin of the CH_4 column increase, an empirical assessment of the data from the whole flight has been performed. From the assessment a linear equation

$$\Delta\mathrm{PSFR}(CH_4/CO_2) = \Delta R \cdot (-0.38) \cdot 10^{-4} \quad (25)$$

was derived by linear regression as first approximation of the dependency between the retrieved difference (ΔPSFR(CH_4/CO_2)) of the normalized CH_4/CO_2 PSF ratio, and the variation of the upwelling radiance ΔR in binary units (BU). The difference in the measured upwelling radiance during the landfill transect was in the order of $\Delta R \approx 2000$–6000 BU (centre – side variations during the transect). Assuming that the observed radiances R (and corresponding detector fillings) are proportional to variations of the albedo/SSR, the resulting albedo/SSR dependent offset of the normalized CH_4/CO_2 PSF ratio for the landfill transect can be estimated to be: ΔPSFR(CH_4/CO_2)≈0.076–0.2280%. The albedo/SSR dependent total column variation ($\Delta AC_{TC,\%}$) is then calculated to

$$\begin{aligned} \Delta AC_{TC,\%}(CH_4) &= \Delta\mathrm{PSFR}(CH_4/CO_2) \cdot c(CH_4) \\ &\approx 0.042 - 0.128\% \end{aligned} \quad (26)$$

offset of the total column. Thus the albedo/SSR dependent variation in the retrieved CH_4 total column is smaller than the retrieved total column increase of ~0.56–1.12% CH_4 during the transect.

AMTD
3, 3199–3276, 2010

7 Summary

The Methane Airborne MAPper (MAMAP) is a new type of passive airborne remote sensing instrument, which measures the back scattered electromagnetic radiation in the spectral regions of the CH_4, CO_2 and O_2 atmospheric absorptions. On inversion using differential optical absorption spectroscopy (DOAS), the reflected (and scattered) solar radiation in the NIR and SWIR spectral range yield the column amounts and dry column amounts of CH_4 and CO_2 and the ratio of CH_4 to CO_2. The instrument has been designed for flexible operation on board of several airborne platforms (e.g., Cessna 207, Cessna Caravan and AWI Polar-5 aircraft). The spectral resolution of the instrument is ~0.82 nm for CH_4 and CO_2 detection (between 1590 nm and 1690 nm) and 0.46 nm for the detection of O_2 (~760 nm). In the current version of the WFMD/M retrieval algorithm simultaneously retrieved CO_2 columns are used to estimate the dry CH_4 air columns and to account for line-of-sight errors. For overflights over strong CO_2 sources (i.e. power plants) also the vice versa approach is applied and the retrieved dry CO_2 air columns are calculated by normalization with the respective measured CH_4 air columns. To test the instrument performance different ground based and airborne measurements on different aircrafts and on the campus of the university of Bremen have been performed. The "on-ground" tests demonstrate that the instrument is able to measure and retrieve with high precision CH_4/CO_2 profile scaling factor ratios (PSFRs) in sun illuminated target (SIT) "pseudo" nadir configuration. In this measurement geometry the instrument observed the radiance of a group of trees illuminated by the Sun. For these measurements a precision of ~0.33% of the CH_4/CO_2 PSF ratio (at 0.148 s exposure times) can be achieved for each single detector exposure. The precision is defined as the standard deviation (1 σ) of the retrieved PSF ratios. The according SNR for each single exposure was in the range of $\overline{\text{SNR}}\approx1600$ (Sect. 4.4). This is in good agreement with model simulations where shot noise, dark signal shot noise and readout noise of the detector are the main contributors.

AMTD
3, 3199–3276, 2010

A second ground test demonstrated that the instrument is able to directly measure scattered down-welling hemispheric radiance. With a f-number of f/3.9, single detector exposure times in the order of 0.7–1 s have been achieved in zenith sky geometry. For these measurements a single readout precision of 0.63% of the retrieved CH_4/CO_2 PSF ratios and $\overline{SNR}$ values of ~1200 have been accomplished. These values were close to the results obtained by instrument model simulations (Sect. 4.4).

It was demonstrated that at an altitude of 4500 m MAMAP reaches an average single readout precision of the retrieved CH_4/CO_2 PSF ratios in the range of ~1.10% (for 0.058 s exposure time) over land targets with homogeneous radiance distribution. Assuming that changes within the concentration only occur in the CH_4 column below the aircraft, this corresponds to a 0.73% CH_4 total column variation. Over water (at 4500 m altitude, albedo/SSR 0.01) with homogeneous radiance an average single readout precision of the retrieved CH_4/CO_2 PSF ratios of 1.12% (for 1 s exposure time) can be obtained (corresponding to ~0.94% CH_4 total column variation). Both PSFR precision estimates are very close to the simulated values of 0.71% for homogeneous land (LHO) and 0.83% for homogeneous water targets (WHO) as summarized in Table 4. The MAMAP precision over these types of targets is limited primarily by shot and detector noise and not affected by vibrations. The estimated airborne short-term spectral stability for these targets is well within the requirements, even though the stability is a factor of ~5.5–20 decreased compared to ground based observations (see Table 5).

For airborne measurements over targets with inhomogeneous surface radiance, the instrument achieves a single readout precision of the retrieved PSF ratios of 2.8% (at 0.058 s exposure time) for land (LIH) and 2.74% (at 1 s exposure time) for water (WIH). Assuming changes in the CO_2 column as constant and CH_4 changes to occur only below the aircraft (altitude of 4500 m), this corresponds to singe readout total column precisions of 1.9% for land (albedo/SSR ~0.18) and 2.5% for water (albedo/SSR ~0.01). These estimated precisions are a factor of 3.9 (land)–6.5 (water) lower compared to model simulations. The degraded performance for inhomogeneous illumination is attributed to smile and keystone effects of the spectrometer system's optical

AMTD
3, 3199–3276, 2010

bench, combined with the resulting inhomogeneous illumination along the slit. Minor effects, like small spectral features in the earthshine spectral reflectance, can not be completely excluded. The assumption that the inhomogeneous slit illumination is primary responsible for the degraded performance was supported and confirmed by ZEMAX® optical design program's end-to-end simulations of the optical system of MAMAP. The assumption is furthermore also supported by the fact, that degraded short-term spectral stability over targets with inhomogeneous radiance can be observed, as compared to those with homogeneous radiance. The origin of this stability degradation can not be traced back to vibrations or thermal changes of the optical bench. A modification of the spectrometer's optical bench incorporating a specially designed spatial scrambler unit is proposed to reduce spectral shifts and slit variations. It is expected that the precision for the CH_4/CO_2 PSF ratio for each single readout can be reduced from currently 2.8% to less than 1.5%. Under the assumption that the precision is barely affected by small spectral structures of the SSR, single readout precisions for the PSFR in the order of 1% remain feasible as can be demonstrated for homogeneous targets (i.e. PSFRP=1.1% for LHO and 1.12% for WHO, corresponding to CH_4 total column precisions of ~0.75% for LHO and ~0.94% for WHO).

For airborne operation in co-added burst mode (BM) the instrument achieved a CH_4/CO_2 profile scaling factor ratio precision $PSFRP_{BM}$ over land targets with inhomogeneous radiance (LIH) of ~1.74% (10 measurements co-added) as summarized in Table 6. For a flight altitude of 4500 m this corresponds to a 1.18% CH_4 total column precision (~180 ppm m), assuming all changes below the aircraft and CO_2 as constant.

For the total co-adding time of 0.6–0.8 s and a cruise speed of ~200 km/h, ground scenes lengths along the flight track (LT) of 33–44 m are achieved. Overall the instrument achieves the target precision of 1–2% total column (corresponding to 150–300 ppm m below the aircraft) for the target ground scene lengths of <200 m (LT) over land for typical albedos/SSR of ~0.18. After modification of the optical bench, total column precisions $\ll$1% for ground scene lengths (LT) <200 m are predicted. In that case the MAMAP CH_4 total column uncertainty variation will no longer be limited by

AMTD
3, 3199–3276, 2010

the precision of the instrument but by the relative accuracy.

In 2007 several flights were performed over anthropogenic targets. It has been demonstrated that MAMAP is able to measure elevated levels of CO_2 downwind from coal-fired power plants. Flights over a landfill with organic waste indicated anomalies in the retrieved CH_4/CO_2 PSFRs (see Sect. 6) within the range of ~1–2%, corresponding to a 0.56–1.12% concentration increase of the total CH_4 column below the aircraft. From this measured anomaly and by knowledge of the wind speed, estimates of the expected fluxes were made using a simple model. With these calculations it can be estimated that the mean emission rate of the landfill for the upper central area must be in the range of 1.24–2.48 g/m^2/h or larger (see Sect. 6).

Using models of the emission, it can also be demonstrated that the achieved instrument precision of ~1% total column at the high spatial resolution enables the CH_4 emissions from strong local sources to be quantified. Such local sources comprise geological sources such as dry seeps and mud volcanoes, the destabilization of shallow gas hydrates, anthropogenic emissions from landfills with organic waste and fugitive emissions from oil and gas industry (i.e. well drilling and abandoned gas wells, oil sand tailings settling basins, emissions from gas and oil processing and gas compression and transport). In addition strong local CO_2 sources such as coal-fired power plants and direct and sub areal emissions from volcanoes can be measured and characterized. Measurements of the emissions from strong and large areal sources such as rice paddies, tropical and Siberia wetlands, will become feasible for periods of large emissions but requires appropriate weather conditions, flight patterns and data averaging strategies. Under stable atmospheric conditions, MAMAP measurements can potentially be used for micro-, meso- and synoptic scale validation of daily CH_4 and CO_2 chemical transport model simulations, and for validation of satellite measurements. Furthermore, MAMAP also serves, as a test bed for future greenhouse gas imaging sensor developments for airborne and space instrumentation, for example like the CarbonSat concept (Bovensmann et al., 2010).

AMTD
3, 3199–3276, 2010

Acknowledgements. We would like especially to thank Ira Leifer, University of California, Santa Barbara (USA), Torsten Sachs, German Research Centre for Geosciences (GFZ), Germany, and Oliver Schneising, University of Bremen (UB), Germany for comments and corrections on the early version of this manuscript.

We would like to thank the mechanical workshops of the German Research Centre for Geosciences (GFZ), and the University of Bremen, especially Ronny Giese (GFZ), Elke Sorgenicht (UB) and Andre Brünkers (UB) for manufacturing the mechanical parts of the MAMAP instrument.

We would like to thank our pilots, especially Carsten Lindemann from Free University Berlin (FUB) for the meteorological support during the campaigns.

MAMAP flights and ground operations were supported in different ways by the German Research Centre for Geosciences (GFZ), Germany; the University and State of Bremen, Germany; Institute for Space Science (ISS), Free University of Berlin (FUB), Germany; Alfred Wegener Institute for Polar and Marine Research (AWI), Germany; Enterprise Airlines, Canada; Lake Central Air Services (LCAS), Canada; Transport Canada (design approval), Canada; RWE Power AG, Germany.

Information on the actual emission of the power plant Schwarze Pumpe and Jänschwalde, Germany were provided by Vattenfall Europe Generation AG & Co. KG, Cottbus, Germany

The solar spectrum used was obtained from NSO / Kitt Peak (http://solarnews.nso.edu) and was produced cooperatively by NSF/NOAO, NASA/GSFC, and NOAA/SEL.

References

Archer, D. and Buffett, B.: Time-dependent response of the global ocean clathrate reservoir to climatic and anthropogenic forcing, Geochem. Geophys. Geosyst., 6, 3, doi:10.1029/2004GC000854, 2005. 3204

Armendariz, A.: Emissions from natural gas production in the Barnett Shale Area and opportunities for cost effective improvements, Report, Peer-Review draft, Department of Environmental and Civil Engineering, Southern Methodist University, Dallas, Texas, 2008. 3207

Barkley, M. P., Frieß, U., and Monks, P. S.: Measuring atmospheric CO_2 from space using Full

AMTD

3, 3199–3276, 2010

Spectral Initiation (FSI) WFM-DOAS, Atmos. Chem. Phys., 6, 3517–3534, doi:10.5194/acp-6-3517-2006, 2006. 3216
Bartlett, K. B. and Harriss, R. C.: Review and assessment of methane emissions from wetlands, Chemosphere, 26, 261–320, doi:10.1016/0045-6535(93)90427-7, 1993. 3205
Baubron, J., Allard, P., and Toutain, J.: Diffuse volcanic emissions of carbon dioxide from Vulcano Island, Italy, Nature, 344, 51–53, 1990. 3206
Bergamaschi, P., Krol, M., Dentener, F., Vermeulen, A., Meinhardt, F., Graul, R., Ramonet, M., Peters, W., and Dlugokencky, E. J.: Inverse modelling of national and European CH_4 emissions using the atmospheric zoom model TM5, Atmos. Chem. Phys., 5, 2431–2460, doi:10.5194/acp-5-2431-2005, 2005 3203
Bergamaschi, P., Frankenberg, C., Meirink, J. F., Krol, M., Dentener, F., Wagner, T., Platt, U., Kaplan, J. O., Körner, S., Heimann, M., Dlugokencky, E. J., and Goede, A.: Satellite chartography of atmospheric methane from SCIAMACHY on board ENVISAT: 2. Evaluation based on inverse model simulations, J. Geophys. Res., 112, 501–511, doi:10.1029/2006JD007268, 2007. 3203, 3205
Bergamaschi, P., Frankenberg, C., Meirink, J. F., Krol, M., Villani, M. G., Houweling, S., Dentener, F., Dlugokencky, E. J., Miller, J. B., Gatti, L. V., Engel, A., and Levin, I.: Inverse modelling of global and regional CH_4 emissions using SCIAMACHY satellite retrievals, J. Geophys. Res., 114, D22301, doi:10.1029/2009JD012287, 2009. 3203
Bohn, T. J., Lettenmaier, D. P., Sathulur, K., Bowling, L. C., Podest, E., McDonald, K., and Friborg, T.: Methane emissions from Western Siberian wetlands: heterogeneity and sensitivity to climate change, Environ. Res. Lett., 2, 045015, doi:10.1088/1748-9326/2/4/045015, 2007. 3239
Börjesson, G., Danielsson, Å., and Svennson, B. H.: Methane fluxes from a Swedish landfill determined by geostatistical treatment of static chamber measurements, Environ. Sci. Technol., 34, 4044–4050, 2000. 3206, 3238, 3243
Bovensmann, H., Burrows, J., Buchwitz, M., Frerick, J., Noël, S., and Rozanov, V.: SCIAMACHY: mission objectives and measurement modes, J. Atmos. Sci., 56, 127–150, 1999. 3203
Bovensmann, H., Buchwitz, M., Burrows, J. P., Reuter, M., Krings, T., Gerilowski, K., Schneising, O., Heymann, J., Tretner, A., and Erzinger, J.: A remote sensing technique for global monitoring of power plant CO_2 emissions from space and related applications, Atmos. Meas. Tech., 3, 781–811, doi:10.5194/amt-3-781-2010, 2010. 3221, 3241, 3242, 3247

AMTD
3, 3199–3276, 2010

Bowen, R. G., Dallimore, S. R., and Côté, M. M.: Geomorphology and Gas Release from Pockmark Features in the Mackenzie Delta, Northwest Territories, Canada, Proceedings 9th International Conference on Permafrost, University of Alaska Fairbanks (http://www.nicop.org/), 1, 171–176, 2008. 3238

Bréon, F.-M. and Ciais, P.: Spaceborne remote sensing of greenhouse gas concentrations, C. R. Geosci., 342, 412–424, doi:10.1016/j.crte.2009.09.012, 2010. 3203, 3204, 3208, 3209, 3236

Buchwitz, M., Rozanov, V. V., and Burrows, J. P.: A near-infrared optimized DOAS method for the fast global retrieval of atmospheric CH_4, CO, CO_2, H_2O, and N_2O total column amounts from SCIAMACHY Envisat-1 nadir radiances, J. Geophys. Res., 105, 15231–15245, 2000. 3203, 3217

Buchwitz, M., de Beek, R., Burrows, J. P., Bovensmann, H., Warneke, T., Notholt, J., Meirink, J. F., Goede, A. P. H., Bergamaschi, P., Körner, S., Heimann, M., and Schulz, A.: Atmospheric methane and carbon dioxide from SCIAMACHY satellite data: initial comparison with chemistry and transport models, Atmos. Chem. Phys., 5, 941–962, doi:10.5194/acp-5-941-2005, 2005a. 3203, 3215, 3217

Buchwitz, M., de Beek, R., Noël, S., Burrows, J. P., Bovensmann, H., Bremer, H., Bergamaschi, P., Körner, S., and Heimann, M.: Carbon monoxide, methane and carbon dioxide columns retrieved from SCIAMACHY by WFM-DOAS: year 2003 initial data set, Atmos. Chem. Phys., 5, 3313–3329, doi:10.5194/acp-5-3313-2005, 2005b. 3203, 3215, 3217

Buchwitz, M., de Beek, R., Noël, S., Burrows, J. P., Bovensmann, H., Schneising, O., Khlystova, I., Bruns, M., Bremer, H., Bergamaschi, P., Körner, S., and Heimann, M.: Atmospheric carbon gases retrieved from SCIAMACHY by WFM-DOAS: version 0.5 CO and CH_4 and impact of calibration improvements on CO_2 retrieval, Atmos. Chem. Phys., 6, 2727–2751, doi:10.5194/acp-6-2727-2006, 2006. 3203

Burlin, Y. K. and Sokolov, B. A.: Russian arctic sedimentary megabasin and its reflection in oil and gas propertries of its borderlands, Polarforschung, 69, 149–154, 2001. 3204

Burrows, J. P., Hölzle, E., Goede, A. P. H., Visser, H., and Fricke, W.: SCIAMACHY – Scanning Imaging Absorption Spectrometer for Atmospheric Chartography, Acta Astronaut., 35, 445–451, 1995. 3203

Chakraborty, S. K. and Anggraini, J.: Massive mud flow and environmental damage following drilling failure – an example from Indonesia, Petrotech–2009, 11–15 January, P09-532, 11–15, 2009. 3238

AMTD
3, 3199–3276, 2010

Chambers, A. and Strosher, M.: DIAL Measurements of Fugitive Emissions from Natural Gas Plants and the Comparison with Emission Factor Estimates, 15th Annual Emission Inventory Conference, US Environmental Protection Agency New Orleans, 15–18 May, 2006a. 3206, 3239

Chambers, A. and Strosher, M.: Refinery Demonstration of Optical Technologies for Measurement of Fugitive Emissions and for Leak Detection, Final Report, Environment Canada, Ontario Ministry of the Environment and Alberta Environment, 2006b. 3206, 3239

Chen, Y.-H. and Prinn, R. G.: Estimation of atmospheric methane emissions between 1996 and 2001 using a three-dimensional global chemical transport model, J. Geophys. Res., 111, D10307, doi:10.1029/2005JD006058, 2006. 3203, 3204, 3205

Chiodini, G., Frondini, F., and Raco, B.: Diffuse emissions of CO_2 from the Fossa crater, Vulcano Island (Italy), B. Volcanol., 58, 41–50, doi:10.1007/s004450050124, 1996. 3206

Crevoisier, C., Nobileau, D., Fiore, A. M., Armante, R., Chédin, A., and Scott, N. A.: Tropospheric methane in the tropics – first year from IASI hyperspectral infrared observations, Atmos. Chem. Phys., 9, 6337–6350, doi:10.5194/acp-9-6337-2009, 2009. 3208

Dimitrov, L.: Contribution to atmospheric methane by natural seepages on the Bulgarian continental shelf, Cont. Shelf Res., 22, 2429–2442, doi:10.1016/S0278-4343(02)00055-9, 2002. 3205

Dlugokencky, E. J., Steele, L. P., Lang, P. M., and Masarie, K. A.: Atmospheric methane at Mauna Loa and Barrow observatories: presentation and analysis of in situ measurements, J. Geophys. Res., 100, 23103–23113, 1995. 3202

Dlugokencky, E. J., Myers, R. C., Lang, P. M., Masarie, K. A., Crotwell, A. M., Thoning, K. W., Hall, B. D., Elkins, J. W., and Steele, L. P.: Conversion of NOAA atmospheric dry air CH_4 mole fractions to a gravimetrically prepared standard scale, J. Geophys. Res., 110, D10307, doi:10.1029/2005JD006035, 2005. 3203

EPER: European Pollutant Emission Register 2004, http://eper.ec.europa.eu/, 2004. 3241, 3242

Ershov, O.: Pergam-Suisse ALMA System Inspection of pipelines from helicopter in the North part of Italy – Report, Pergam-Suisse AG Talacker 42 Zürich 8001, Switzerland, 2007. 3207

Etiope, G.: Natural emissions of methane from geological seepage in Europe, Atmos. Environ., 43, 1430–1443, doi:10.1016/j.atmosenv.2008.03.014, 2009. 3205

Etiope, G., Feyzullayev, A., Baciu, C. L., and Milkov, A. V.: Methane emission from mud volcanoes in Eastern Azerbaijan, Geology, 32, 465–468, doi:10.1130/G20320.1, 2004. 3205,

AMTD
3, 3199–3276, 2010

3238
Etiope, G., Fridriksson, T., Italiano, F., Winiwarter, W., and Theloke, J.: Natural emissions of methane from geothermal and volcanic sources in Europe, J. Volcanol. Geoth. Res., 165, 76–86, doi:10.1016/j.jvolgeores.2007.04.014, 2007. 3205
Etioppe, G. and Klusman, R. W.: Geologic emissions of methane to the atmosphere, Chemosphere, 49(8), 777–789, doi:10.1016/S0045-6535(02)00380-6, 2002. 3205
Etioppe, G. and Klusman, R. W.: New Directions: GEM – Geologic Emissions of Methane, the missing source in the atmospheric methane budget, Atmos. Environ., 38, 3099–3100, doi:10.1016/S0045-6535(02)00380-6, 2004. 3205
Fellner, J., Schöngrundner, P., and Brunner, P. H.: Methanemissionen aus Deponien – Bewertung von Messdaten (METHMES) (durchgeführt im Auftrag des Bundesministeriums für Land- und Forstwirtschaft, Umwelt und Wasserwirtschaft), Technische Universität Wien, Institut für Wassergüte und Abfallwirtschaft, Abteilung Abfallwirtschaft und Stoffhaushalt, A-1040 Wien, Karlsplatz 13/226.4, 2003. 3238, 3243
Frankenberg, C., Meirink, J., Weele, M., Platt, U., and Wagner, T.: Assessing methane emissions from global space-borne observations, Science, 308, 1010–1014, doi:10.1126/science.1106644, 2005. 3203, 3216, 3217
Fung, I., John, J., Lerner, J., Matthews, E., Prather, M., Steele, L. P., and Fraser, P. J.: Three-dimensional model synthesis of the global methane cycle, J. Geophys. Res., 96, 13033–13065, 1991. 3205
Gramberg, S., Kulakov, Y. N., Pogrebitsky, Y. E., and Sorokov, D. S.: Arcti Oil and Gas Super Basin, Worl Petroleum Congress, London, 93–99, 1983. 3204
IPCC, 2001: Climate Change 2001: The Scientific Basis, Contribution of Working Group I to the Third Assessment Report of the Intergovernmental Panel on Climate Change, edited by: Houghton, J. T., Ding, Y., Griggs, D. J., Noguer, M., van der Linden, P. J., Dai, X., Maskell, K., and Johnson, C. A., Cambridge University Press, Cambridge, 881 pp, United Kingdom and New York, NY, USA, 2001. 3202
IPCC, 2007: Climate Change 2007: The Physical Science Basis, Contribution of Working Group I to the Fourth Assessment Report of the Intergovernmental Panel on Climate Change, edited by: Solomon, S., Qin, D., Manning, M., Chen, Z., Marquis, M., Averyt, K. B., Tignor, M., and Miller, H. L., Cambridge University Press, Cambridge, 996 pp., United Kingdom and New York, NY, USA, 2007. 3202
Italiano, F., Pecoraino, G., and Nuccio, P. M.: Steam output from fumaroles of an active volcano:

AMTD
3, 3199–3276, 2010

tectonic and magmatic-hydrothermal controls on the degassing system at Vulcano (Aeolian arc), J. Geophys. Res, 103, 29829–29842, doi:10.1029/98JB02237, 1998. 3206

Jagovkina, S. V., Karol, I. L., Zubov, V. A., Lagun, V. E., Reshetnikov, A. I., and Rozanov, E. V.: Reconstruction of the methane fluxes from the West Siberia gas fields by the 3-D regional chemical transport model, Atmos. Environ., 34, 5319–5328, doi:10.1016/S1352-2310(00)00347-2, 2000. 3203, 3238, 3239

Jagovkina, S. V., Karol, I. L., Zubov, V. A., Lagun, V. E., Reshetnikov, A. I., and Rozanov, E. V.: Methane fluxes in West Siberia: 3-D regional model simulation, Water, Air and Soil Poll., 1, 429–436, doi:10.1023/A:1013106011265, 2001. 3203, 3208, 3239

Judd, A. G.: Natural seabed gas seeps as sources of atmospheric methane, Environ. Geol., 46, 988–996, doi:10.1007/s00254-004-1083-3, 2004. 3238

Khalil, M. A. K.: Atmospheric methane: an introduction, in: Atmospheric Methane: Its Role in the Global Environment, edited by: Khalil, M. A. K., Springer, New York, 1–8, 2008. 3205

Kort, E. A., Eluszkiewicz, J., Stephens, B. B., Miller, J. B., Gerbig, C., Nehrkorn, T., Daube, B. C., Kaplan, J. O., Houweling, S., and Wofsy, S. C.: Emissions of CH_4 and N_2O over the United States and Canada based on a receptororiented modeling framwork and COBRA-NA atmospheric observations, Geophys. Res. Lett., 35, L18808, doi:10.1029/2008GL034031, 2008. 3203

Krings, T., Buchwitz, M., Gerilowski, K. et al.: MAMAP – a new spectrometer system for column-averaged methane and carbon dioxide observations from aircraft: retrieval algorithm and first inversions for point source emission rates, in preparation, 2010. 3237

Livingston, W. and Wallace, L.: An atlas of the solar spectrum in the infrared from 1850 to 9000 cm^{-1} (1.1 to 5.4 µm), National Solar Observatory, Tech. rep. 91-001, 1991. 3218

Matsueda, H. and Inoue, H. Y.: Aircraft measurements of trace gases between Japan and Singapore in October of 1993, 1996 and 1997, Geophys. Res. Lett., 26, 2413–2416, doi:10.1029/1999GL900089, 1999. 3203

Meyer, O., Busack, V., Haepe, S., Theopold, F., and Heimes, F. J.: HELPCOS The Helicopter Based Pipeline Control System of VGN – Verbundnetz AG, 23rd World Gas Conference, Amsterdam, 2006. 3207, 3208

Miller, J. B., Gatti, L. V., d'Amelio, M. T. S., Crotwell, A. M., Dlugokencky, E. J., Bakwin, P., Artaxo, P., and Tans, P. P.: Airborne measurements indicate large methane emissions from the Eastern Amazon Basin, Geophys. Res. Lett., 34, L18808, doi:10.1029/2006GL029213, 2007. 3203

AMTD
3, 3199–3276, 2010

Mörner, N.-A. and Etiope, G.: Carbon degassing from the lithosphere, Global Planet. Change, 33, 185–203, doi:10.1016/S0921-8181(02)00070-X, 2002. 3205, 3239
Nisbet, E.: Methane Monitoring in the European region – MethMonitEUr, EC contract EVK2-CT-2002-00175, Coordinator: Euan Nisbet, Final Report, 2005. 3203
Oberlander, E. A., Brenninkmeijer, C. A. M., Crutzen, P. J., Elansky, N. F., Golitsyn, G., Granberg, I. G., Scharffe, D., Hofmann, R., Belikov, I. B., Paretzke, H. G., and van Velthoven, P. F. J.: Trace gas measurements along the Trans-Siberian railroad: the TROICA 5 expedition, J. Geophys. Res., 107, 4206, doi:10.1029/2001JD000953, 2002. 3203
Rice, A. L., Tyler, S. C., McCarthy, M. C., Boering, K. A., and Atlas, E.: Carbon and hydrogen isotopic compositions of stratospheric methane: 1. High-precision observations from the NASA ER-2 aircraft, J. Geophys. Res., 108, 4206, doi:10.1029/2002JD003042, 2003. 3202
Roberts, D. A., Bradley, E. S., Cheung, R., Leifer, I., Dennison, P. E., and Margolis, J. S.: Mapping methane emissions from a marine geological seep source using imaging spectrometry, Remote Sens. Environ., 114, 592–606, doi:10.1016/j.rse.2009.10.015, 2010. 3207, 3208, 3209
Rothman, L., Jaquemart, D., Barbe, A., Benner, D. C., Birk, M., Brown, L., Carleer, M., Jr, C. C., Chance, K., Coudert, L., Dana, V., Devi, V., Flaud, J.-M., Gamache, R., Goldman, A., Hartmann, J.-M., Jucks, K., Makim, A., Mandin, J.-Y., Massie, S., Orphalh, J., Perrin, A., Rinsland, C., Smith, M., Tennyson, J., Tolchenov, R., Toth, R., Auwera, J. V., Varanasi, P., and Wagner, G.: The Hitran 2004 molecular spectroscopic database, J. Quant. Spectrosc. Ra., 96, 139–204, doi:10.1016/j.jqsrt.2004.10.008, 2005. 3218
Rozanov, A., Rozanov, V., Buchwitz, M., Kokhanovsky, A., and Burrows, J.: SCIATRAN 2.0 – a new radiative transfer model for geophysical applications in the 175–2400 nm spectral region, Adv. Space Res., 36, 1015–1019, doi:10.1016/j.asr.2005.03.012, 2005. 3218, 3240
Sachs, T., Giebels, M., Wille, C., Kutzbach, L., and Boike, J.: Methane Emissions from Siberian Wet Polygonal Tundra on Multiple Spatial Scales: Vertical Flux Measurements by Closed Chambers and Eddy Covariance, Samoylov island, Lena River Delta, Proceedings of the 9th International Conference on Permafrost, University of Alaska, Fairbanks, 29 June–3 July, 1549–1554, 2008. 3202, 3239
Schneising, O.: Analysis and interpretation of satellite measurements in the near-infrared spectral region: atmospheric carbon dioxide and methane, PhD thesis,, University of Bremen, Institute of Environmental Physics (IUP), Germany, 2009. 3217, 3237
Schneising, O., Buchwitz, M., Burrows, J. P., Bovensmann, H., Reuter, M., Notholt, J., Macatan-

AMTD
3, 3199–3276, 2010

gay, R., and Warneke, T.: Three years of greenhouse gas column-averaged dry air mole fractions retrieved from satellite – Part 1: Carbon dioxide, Atmos. Chem. Phys., 8, 3827–3853, doi:10.5194/acp-8-3827-2008, 2008. 3203, 3215, 3216, 3217

Schneising, O., Buchwitz, M., Burrows, J. P., Bovensmann, H., Bergamaschi, P., and Peters, W.: Three years of greenhouse gas column-averaged dry air mole fractions retrieved from satellite – Part 2: Methane, Atmos. Chem. Phys., 9, 443–465, doi:10.5194/acp-9-443-2009, 2009. 3203, 3215, 3216, 3217, 3237

Shakhova, N., Semiletov, I., Salyuk, A., Yusupov, V., Kosmach, D., and Gustafsson, Ö.: Extensive methane venting to the atmosphere from sediments of the East Siberian arctic shelf, Science, 327, 1246–1250, doi:10.1126/science.1182221, 2010. 3204, 3238

Shakhova, N. E., Semiletov, I. P., Salyuk, A. N., Bel'cheva, N. N., and Kosmach, D. A.: Methane anomalies in the near-water atmospheric layer above the shelf of East Siberian arctic shelf, Dokl. Earth Sci., 415, 764–768, doi:10.1134/S1028334X07050236, 2007. 3204

Siddique, T., Gupta, R., Fedorak, P. M., MacKinnon, M. D., and Foght, J. M.: A first approximation kinetic model to predict methane generation from an oil sands tailings settling basin, Chemosphere, 72, 1573–1580, doi:10.1016/j.chemosphere.2008.04.036, 2008. 3239

Suto, H., Kuze, A., Nakajima, M., Hamazaki, T., Yokota, T., and Inoue, G.: Airborne SWIR FTS for GOSAT validation and calibration (Proceedings Paper), SPIE Proceedings, 7106, 1060M, doi:10.1117/12.799963, 2008. 3207, 3208

Takeuchi, W., Tamura, M., and Yasuoka, Y.: Estimation of methane emission from West Siberian wetland by scaling technique between NOAA AVHRR and SPOT HRV, Remote Sens. Environ., 85, 21–29, doi:10.1016/S0034-4257(02)00183-9, 2003. 3202

Villani, M. G., Bergamaschi, P., Krol, M., Meirink, J. F., and Dentener, F.: Inverse modeling of European CH_4 emissions: sensitivity to the observational network, Atmos. Chem. Phys., 10, 1249–1267, doi:10.5194/acp-10-1249-2010, 2010. 3203, 3204

Walter, K. M., Zimov, S. A., Chanton, J. P., Verbyla, D., and Chapin III, F. S.: Methane bubbling from Siberian thaw lakes as a positive feedback to climate warming, Science, 443, 71–75, doi:10.1038/nature05040, 2006. 3204

Walter, K. M., Smith, L. C., and Chapin III, F. S.: Methane bubbling from northern lakes: present and future contributions to the global methane budget, Philos. T. Roy. Soc. A, 365, 1657–1676, doi:10.1098/rsta.2007.2036, 2007. 3204, 3205

Watson, R. T., Rohde, H., Oescherger, H., and Siegenthaler, U.: Greenhouse gases and aerosols, in: Climate Change: The Intergovernmental Panel on Climate Change Scientific

AMTD
3, 3199–3276, 2010

Assessment, edited by: Houghton, J. T., Jenkins, G. J., and Ephraumus, J. J., Cambridge University Press, Cambridge University Press, Cambridge, 1–40, 1990. 3202, 3205

Winderlich, J., Chen, H., Höfer, A., Gerbig, C., Seifert, T., Kolle, O., Kaiser, C., Lavrič, J. V., and Heimann, M.: Continuous low-maintenance $CO_2/CH_4/H_2O$ measurements at the Zotino Tall Tower Observatory (ZOTTO) in Central Siberia, Atmos. Meas. Tech. Discuss., 3, 1399–1437, doi:10.5194/amtd-3-1399-2010, 2010. 3203

Wuebbles, D. J. and Hayhoe, K.: Atmospheric methane and global change, Earth-Sci. Rev., 57, 177–210, doi:10.1016/S0012-8252(01)00062-9, 2002. 3202, 3204, 3206, 3207

Yoshida, J., Kawashima, T., Ishida, J., Hamada, K., Tanii, J., Katsuyama, Y., Suto, H., Kuze, A., Nakajima, M., and Hamazaki, T.: Prelaunch performance test results of TANSO-FTS and CAI on GOSAT (Proceedings Paper), Proc. SPIE, 7082, doi:10.1117/12.800701, 2008. 3203, 3208

Zimig, W. and Ulbricht, M.: CHARM® – The dawn of a new era in checking the tightness of natural gas pipelines, 23rd World Gas Conference, Amsterdam, 2006. 3207

AMTD
3, 3199–3276, 2010

Table 1. MAMAP sensor parameters.

CH_4/CO_2-SWIR-spectrometer	O_2-NIR-spectrometer
F = 300 mm temperature stabilized grating spectrometer system (f/3.9) *Grating*: 600 grooves/mm *Detector*: LN cooled 1024 pixel InGaAs FPA *Spectral range*: ~1.590–1.690 nm *Spectral resolution*: ~0.82 nm FWHM *Spectral sampling*: ~8.6 pixel / FWHM *Detector-SNR*: ~1000 at ~0.6–0.8 s integration time (10 detector readouts co-added, surface albedo/SSR 0.18) *IFOV*: ~1.34° across track (CT) × ~0.02° along track (LT) *Spatial resolution*: At 1 km flight height, ground speed 200 km/h the co-added ground pixel size is in the order of 33 m along track over land (surface albedo/SSR 0.18) and larger for lower albedo/SSR surfaces. Across track the pixel size is in the order of 23.4 m	*F* = 300 mm temperature stabilized push broom imaging grating spectrometer system (f/3.9) *Grating*: 1200 grooves/mm *Detector*: 512 × 512 pixel CCD Sensor, TE cooled, 6 pixel binned in imaging direction and 2 in spectral direction *Spectral range*: ~756–769 nm *Spectral resolution*: ~0.46 nm FWHM *Spectral sampling*: ~9 pixel / FWHM *Detector-SNR*: >4000 (binned) at ~0.6–0.8 s integration time (10 detector readouts co-added, 1/4 of the 85 spatial rows binned, surface albedo/SSR 0.18) *IFOV*: ~5.85° across track (CT, divided into 85 pixel) × ~0.072° along track (LT) *Spatial resolution*: At 1 km flight height, ground speed of 200 km/h the co-added ground pixel size is on the order of 33 m along track over land (surface albedo/SSR 0.18) and larger for lower albedo/SSR surfaces. Across track the pixel size is in the order of 102.2 m (divided by 85)
Precision requirement: Goal: better than 1% of the total CH_4 over CO_2 column-averaged dry air mixing ratio with respect to the atmospheric background; threshold: better than 2% (precision is defined as the random error of the retrieved CH_4 and CO_2 columns due to instrument noise) *Size*: 2 "Falcon" standard racks, 556 mm × 650 mm × 968 mm each *Weight*: ~120 kg (each rack) *Power consumption*: ~600–800 Watt at nominal operation, <1000 Watt at warm-up	

AMTD
3, 3199–3276, 2010

Table 2. MAMAP total column conversion factors c for retrieval output profile scaling factors (PSF), assuming all deviations from mean column occurred below the aircraft. All conversion factors were computed based on SCIATRAN RTM simulations.

Airplane altitude [m]	Solar zenith angle [°]	Surface albedo [–]	Conversion Factor c [–] CH_4	CO_2
850	40	0.01	0.575	0.459
850	40	0.05	0.546	0.435
850	40	0.18	0.535	0.426
850	50	0.01	0.607	0.478
850	50	0.05	0.571	0.448
850	50	0.18	0.558	0.438
1250	40	0.18	0.550	0.440
4500	40	0.01	0.839	0.681
4500	40	0.05	0.703	0.568
4500	40	0.18	0.667	0.538
4500	50	0.01	0.893	0.714
4500	50	0.05	0.725	0.577
4500	50	0.18	0.680	0.540

AMTD
3, 3199–3276, 2010

Table 3. MAMAP reference targets data set selected for precision estimates.

Abbreviation	Target	Observation conditions	Illumination of slit	Observation geometry
WHO	water radiance	dynamic (in-flight)	homogeneous, slight dynamic changes	nadir
WIH	water radiance	dynamic (in-flight)	inhomogeneous, dynamic changes	nadir
LHO	land radiance	dynamic (in-flight)	inhomogeneous, slight dynamic changes	nadir
LIH	land radiance	dynamic (in-flight)	inhomogeneous, dynamic changes	nadir
ZIR	solar+hemispheric radiance and irradiance	dynamic (in-flight)	homogeneous, changes only in intensity	zenith (over 3 transmissive diffusers+ fiber
ZRG	zenith radiance	static (on-ground)	homogeneous, slight variations in aerosols and clouds	zenith
SIT	sun illuminated target, radiance	static (on-ground)	inhomogeneous, static no changes	SIT (quasi nadir)

AMTD
3, 3199–3276, 2010

Table 4. Simulated and measured MAMAP SWIR single readout detector performance for different reference targets including on-ground and in-flight measurements. The table includes the exposure time t_{exp} (column 3), the simulated and measured signal in [BU] (column 4 and 5), the simulated and retrieved SNR (column 6 and 7), the simulated profile scaling factor precision (PSFP) for each gas (column 8) and the simulated and (from measurements) mean retrieved profile scaling factor ratio precision (PSFRP) calculated from the CH_4/CO_2 PSF ratios (column 9 and 10).

Target	Gas	t_{exp} [s]	Signal (sim) [BU]	$\overline{\text{Signal}}$ (meas) [BU]	$\overline{\text{SNR}}$ (sim) [–]	$\overline{\text{SNR}}$ (ret) [–]	PSFP (sim) [%]	PSFRP (sim) [%]	PSFRP (ret) [%]
WHO	CO_2	1.000	9230	12 158	542	411	0.69	0.83	1.12
WHO	CH_4	1.000	9130		533	422	0.47		
WIH	CO_2	1.000	24 000	26 612	1063	598	0.35	0.42	2.74
WIH	CH_4	1.000	23 435		1047	532	0.24		
LHO	CO_2	0.058	9636	11 480	638	588	0.59	0.71	1.10
LHO	CH_4	0.058	9410		628	538	0.39		
LIH	CO_2	0.058	9636	11 618	638	475	0.59	0.71	2.80
LIH	CH_4	0.058	9410		628	418	0.39		
ZIR	CO_2	0.400	9969	10 814	621	620	0.60	0.72	0.59
ZIR	CH_4	0.400	9734		611	570	0.41		
ZRG	CO_2	0.700	33 600	33 349	1338	1290	0.28	0.33	0.63
ZRG	CH_4	0.700	32 890		1319	1181	0.19		
SIT	CO_2	0.148	43 716	45 614	1605	1651	0.23	0.27	0.33
SIT	CH_4	0.148	42 000		1584	1566	0.15		

AMTD
3, 3199–3276, 2010

Table 5. MAMAP SWIR relative single readout detector spectral stability (readout to readout) as retrieved by best estimate of the WFMD/M algorithm for different reference targets for a slit function FWHM of 0.82 nm. The different stability values are not directly comparable because of different exposure times during the measurements. Comparison of the shift values for different conditions give only a raw estimate for short time spectral shifts caused by vibrations and short time spectral shifts caused by inhomogeneous illumination of the slit induced by keystone and smile effects of the spectrometer.

Target	t_{exp} [s]	SDEV spectral shift [nm]	SDEV spectral shift [%]	Observation conditions
WHO	1.000	0.0049	0.60	dynamic (in flight)
WIH	1.000	0.0101	1.23	dynamic (in flight)
LHO	0.058	0.0180	2.20	dynamic (in flight)
LIH	0.058	0.0364	4.45	dynamic (in flight)
ZIR	0.400	0.0041	0.50	dynamic (in flight)
ZRG	0.700	0.0017	0.21	static (on ground)
SIT	0.148	0.0009	0.11	static (on ground)

AMTD
3, 3199–3276, 2010

Table 6. MAMAP in-flight SWIR detector performance over inhomogeneous land targets (LIH) for co-added burst mode. The table include the simulated and retrieved SNR of the instrument for 10 co-added burs mode (BM) measurements (column 4 and 5) and also the simulated and (from measurements) retrieved CH_4/ CO_2 PSF ratio precision ($PSFRP_{BM}$) in column 6 and 7.

Target	Gas	T_{int} [s]	$\overline{SNR}_{BM}$ (sim) [–]	$\overline{SNR}_{BM}$ (ret) [–]	$PSFRP_{BM}$ (sim) [%]	$PSFRP_{BM}$ (ret) [%]
LIH	CO_2	0.58	2017	957	0.225	1.74
LIH	CH_4	0.58	1986	827		

AMTD
3, 3199–3276, 2010

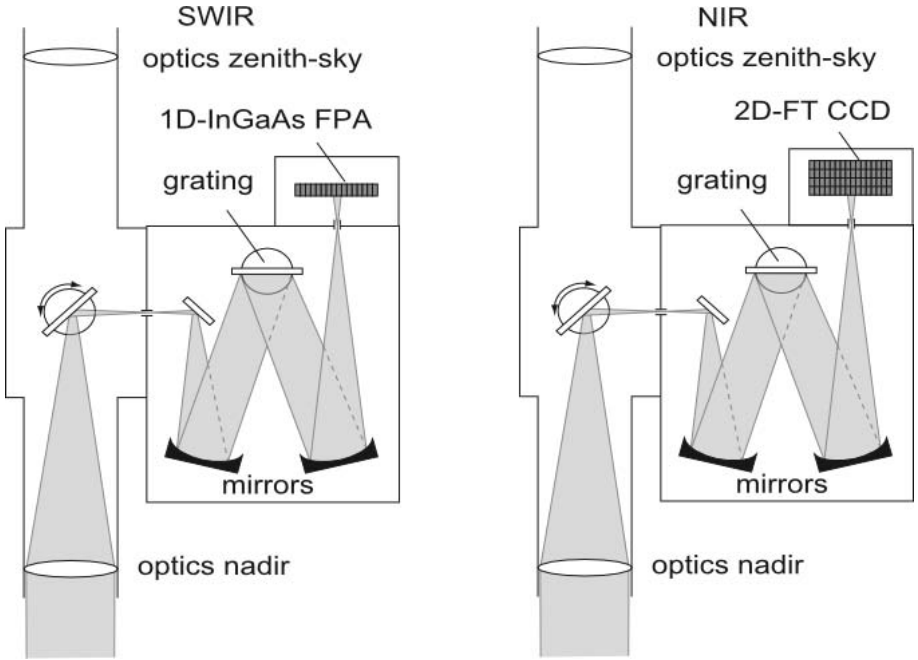

Fig. 1. Sketch of the MAMAP SWIR and NIR spectrometer modules. Both spectrometers have two separate light intake telescopes pointing towards nadir and zenith-sky directions for measurements of nadir and zenith radiances. A mirror enables switching between both modes. For zenith irradiance measurements zenith optics can be equipped optionally with glass fibers and transmissive diffuser optical inlets (not shown in this sketch).

AMTD
3, 3199–3276, 2010

MAMAP – a new spectrometer system: instrument description

K. Gerilowski et al.

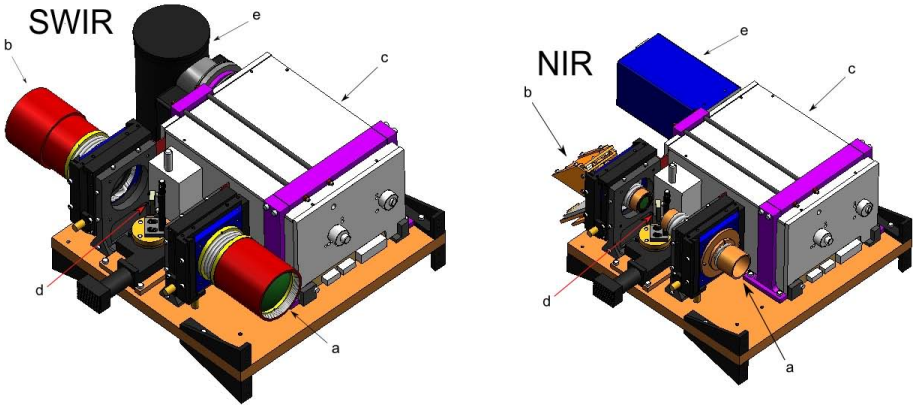

Fig. 2. CAD drawing of the SWIR (left) and NIR (right) spectrometer modules. **(a)** nadir optics, **(b)** zenith-sky optics (equipped with telescopes for radiance measurements), **(c)** spectrometer housing, **(d)** automated fold mirror, **(e)** SWIR/NIR detector heads.

AMTD
3, 3199–3276, 2010

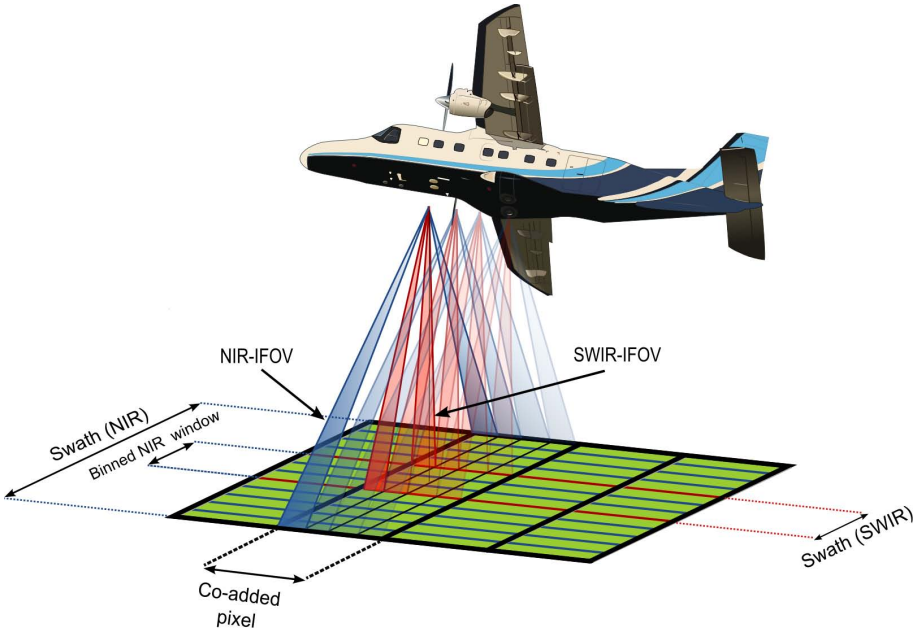

Fig. 3. MAMAP observation geometry for the 1-D-SWIR (red) and the 2-D imaging NIR (blue) spectrometer.

AMTD
3, 3199–3276, 2010

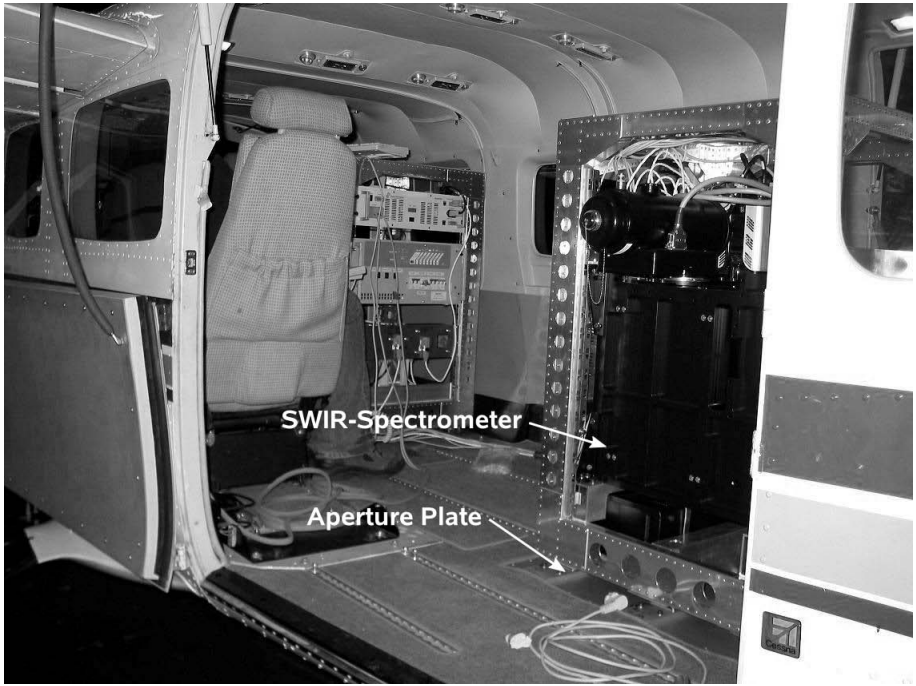

Fig. 4. The MAMAP spectrometer rack mounted on the aperture-plate (front) carrying the optics and the spectrometer systems and the MAMAP auxiliary rack (back) carrying the controllers, power converters and the buffer battery (both racks mounted on the RWE Cessna caravan aircraft).

AMTD
3, 3199–3276, 2010

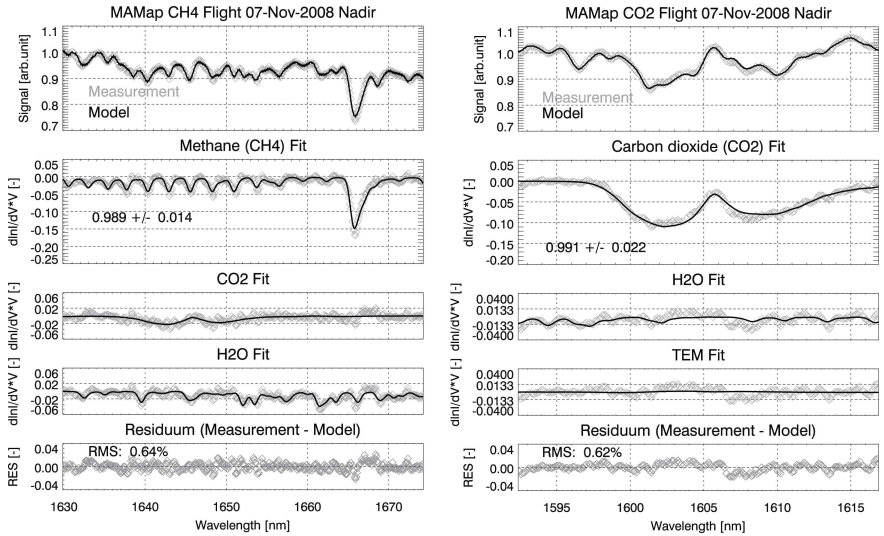

Fig. 5. WFM-DOAS fits in the spectral regions used for CH_4 (left) and CO_2 (right) retrieval. The MAMAP spectral measurements have been made on 07 Nov 2008 during the flight from Oshawa to Wilmington, USA, on board of the Polar-5 aircraft of the Alfred-Wegener-Institute (AWI), Bremerhaven, Germany. Left: The top panel shows a MAMAP nadir spectrum (grey symbols) and the solid line the fitted linearized radiative transfer model. The bottom panel shows the fit residuum, which is the difference between measurement and simulation after the fit (the root-mean-square (RMS) of the fit residuum (RES) is 0.64%). The second panel shows details of the methane fit. The solid line is the scaled derivative of the radiance with respect to a change of the methane vertical column. The retrieved scaling factor for the methane vertical profile is 0.989±0.014, i.e., the retrieved columns is 1.1% lower than the vertical column which has been assumed for the radiative transfer simulations. The grey symbols show the "methane fit residuum", which is identical with the black curve except that the spectral fit residuum has been added. The third and the fourth panel show the corresponding results for the interfering gases CO_2 and H_2O. Right: Similar as left figure but for the CO_2 fitting window.

AMTD
3, 3199–3276, 2010

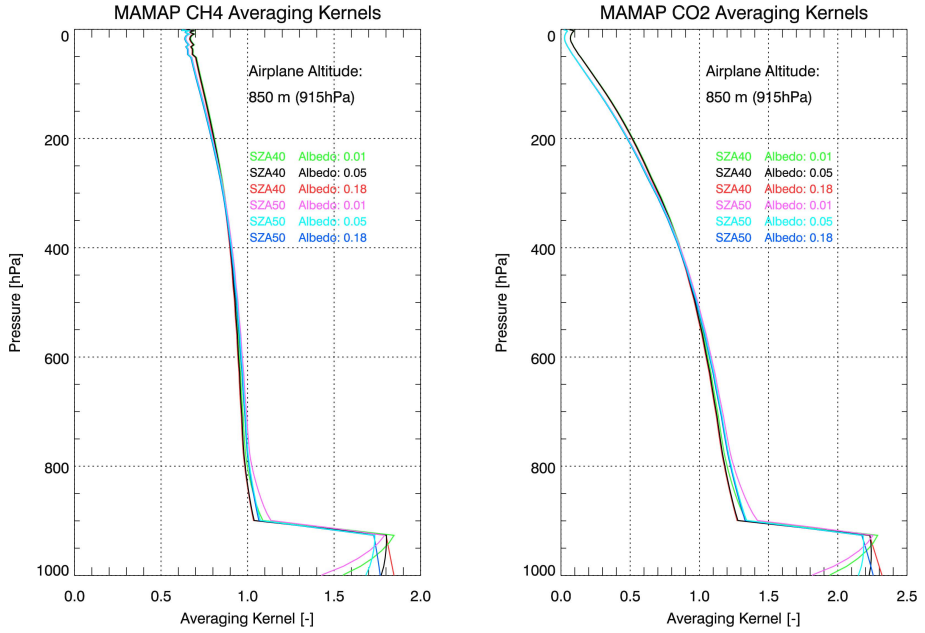

Fig. 6. Averaging kernels for the MAMAP instrument depending on solar zenith angle (SZA) and surface albedo/SSR for a nadir measurement at 850 m flight altitude. The figure shows the striking difference of the averaging kernels below the instrument compared to above the instrument This difference is due to the fact that for a nadir viewing instrument light coming from the sun passes through the absorber below the aircraft twice (once before and once after reflection at the surface). Left: Averaging kernels for CH_4; Right: Averaging kernels for CO_2.

AMTD
3, 3199–3276, 2010

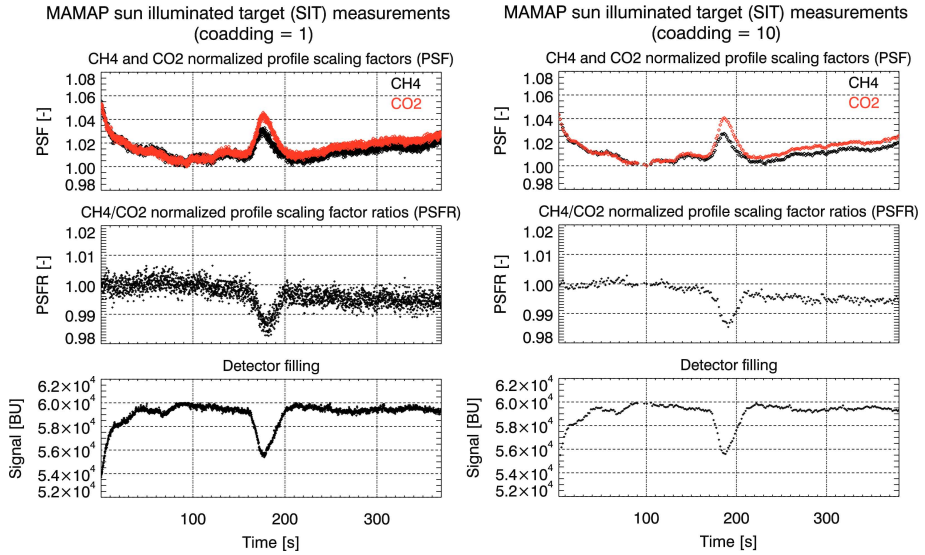

Fig. 7. Analysis of time series of MAMAP CH_4 and CO_2 measurements for slightly variable atmospheric conditions due to thin clouds for the 11 May 2006 stationary "on-ground" sun illuminated target (SIT) measurements. Left: Top panel: Normalized single readout CH_4 (black) and CO_2 (red) profile scaling factors (PSF). Second panel: Normalized single readout CH_4/CO_2 profile scaling factor ratio (PSFR). Bottom panel: maximum radiance (detector filling) in binary units [BU] as measured with MAMAP and digitalized with 16 Bit ADC. Right: As on left side but for 10 readouts co-added to one measurement.

AMTD
3, 3199–3276, 2010

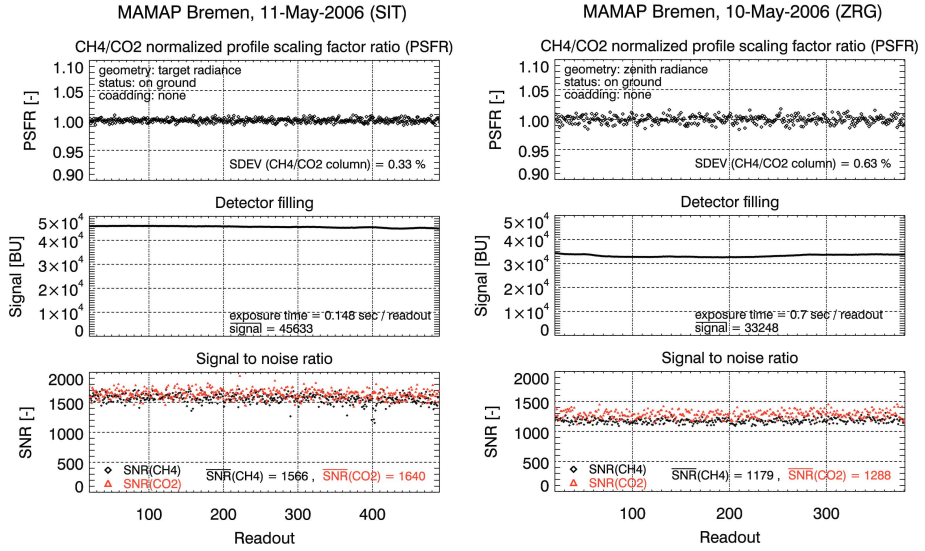

Fig. 8. Analysis of time series of MAMAP single detector readout CH_4 and CO_2 measurements (Left: For the 11 May 2006, Bremen stationary "on-ground" sun illuminated target (SIT) measurements, Right: For the 10 May 2006 "on-ground" zenith sky scattered radiance (ZRG) measurements). Left: Top panel: Normalized CO_2/CH_4 profile scaling factor ratios ($PSFR_i$). Second panel: Maximum radiance (detector filling) in binary units [BU] as measured with MAMAP and digitalized with 16 Bit ADC. Bottom panel: Estimated signal-to-noise ratios (SNR) of the single measurements. Right: As on left side but for the zenith sky scattered radiance measurements (only measurements with >3000 [BU] are processed).

AMTD
3, 3199–3276, 2010

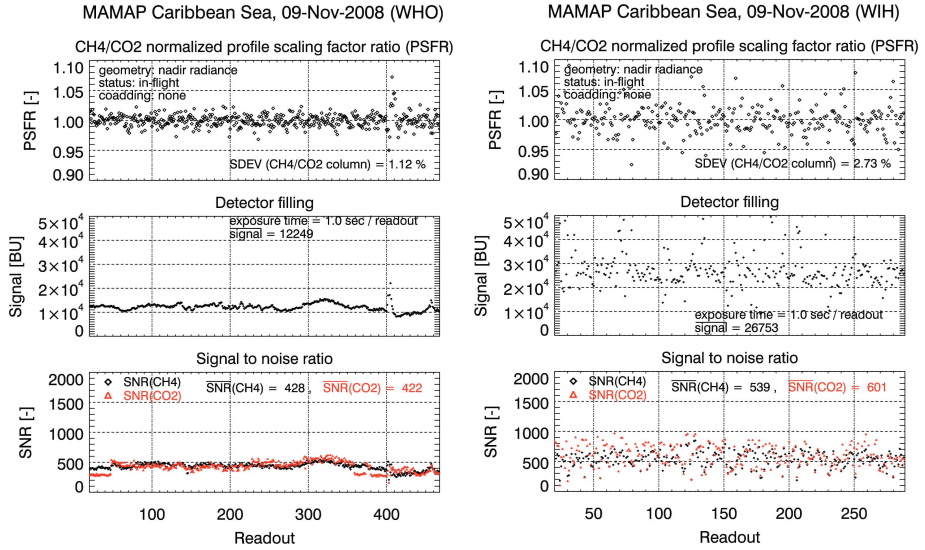

Fig. 9. As Fig. 8 but for in-flight nadir measurements over water; left: Scene with homogeneous reflectance distribution (target WHO); right: Scenes with inhomogeneous reflectance distribution (target WIH).

AMTD
3, 3199–3276, 2010

MAMAP – a new spectrometer system: instrument description

K. Gerilowski et al.

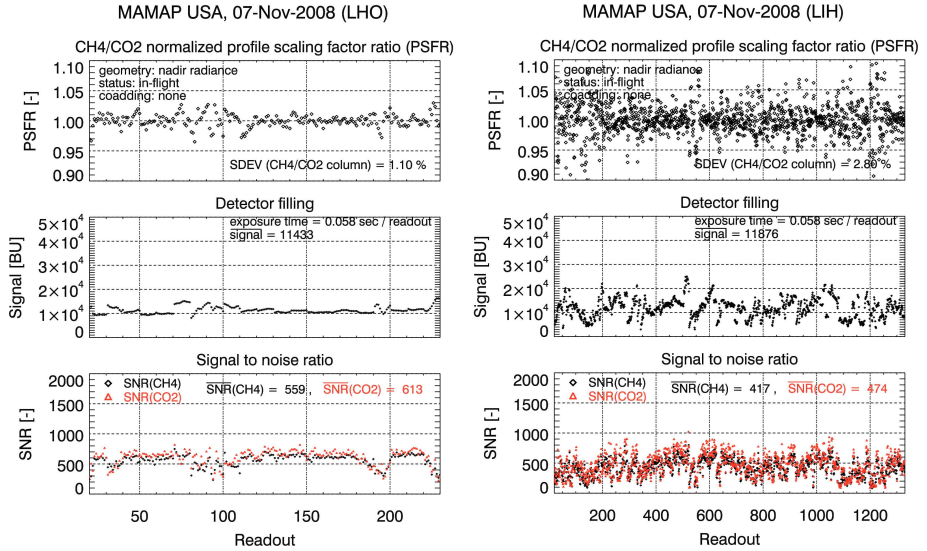

Fig. 10. As Fig. 8 but for in-flight nadir measurements over land; left: Scene with homogeneous reflectance distribution (target LHO); right: Scenes with inhomogeneous reflectance distribution (target LIH).

AMTD
3, 3199–3276, 2010

MAMAP – a new spectrometer system: instrument description

K. Gerilowski et al.

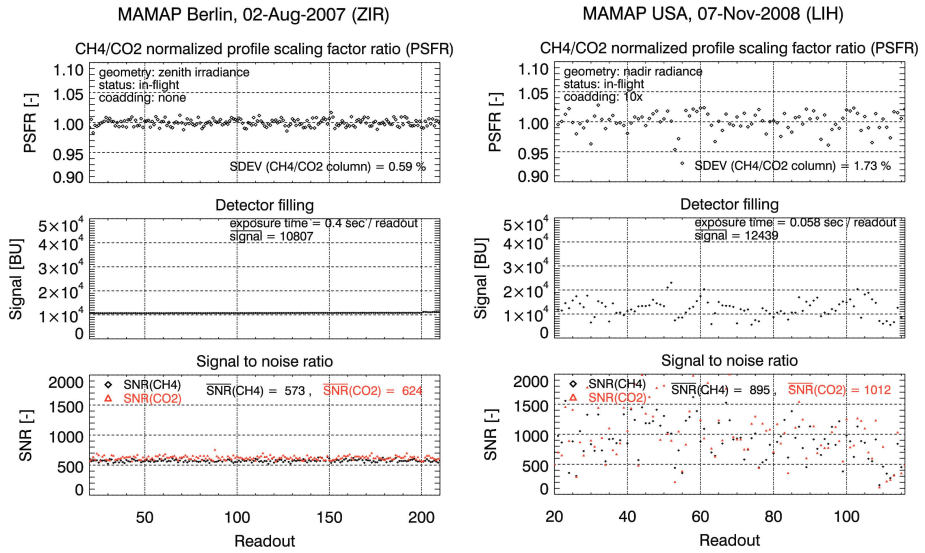

Fig. 11. As Fig. 8 but for in-flight measurements in zenith geometry and for nadir measurements over targets with inhomogeneous reflectance distribution; Left: Analysis of time series of single detector readout MAMAP CH_4 and CO_2 dynamic "in-flight" zenith sky irradiance measurements (solar+hemispheric). Measurements performed over the MAMAP fiber optical inlet equipped with 4 transmissive Spectralon diffuser plates (target ZIR). Measurements conducted on 2 Aug 2007. Top panel: Normalized CO_2/CH_4 profile scaling factor ratio (PSFR). Second panel: Maximum irradiance (detector filling) in binary units [BU] as measured with MAMAP and digitalized with 16 Bit ADC. Bottom panel: Estimated signal-to-noise ratios (SNR) of each measurements; Right: As on left side but for co-added burst mode nadir measurements over land targets with inhomogeneous reflectance distribution (target LIH). Co-added measurements derived from measurements shown in fig 10 (right) but each burst of 10 measurements co-added and averaged (only measurements with >3000 [BU] are processed).

AMTD
3, 3199–3276, 2010

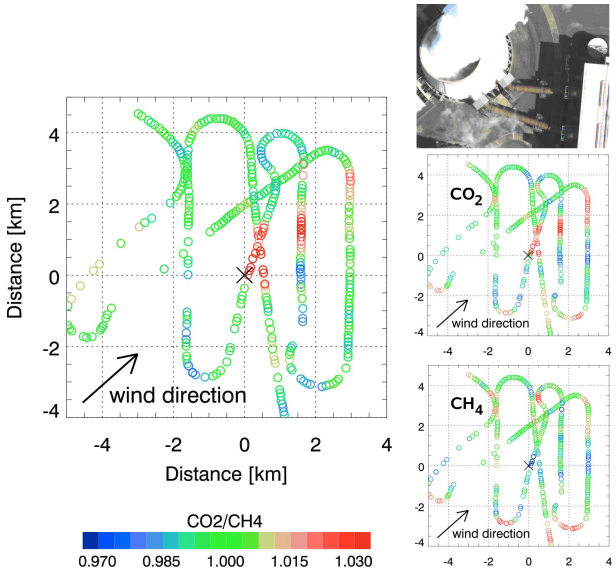

Fig. 12. Left: Normalized MAMAP CO_2/CH_4 profile scaling factor ratio ($PSFR_{BM}$) retrieved from measurements acquired on 26 Jul 2007 over the power plant Jänschwalde (black cross) located north of Cottbus (south-east of Berlin) in Eastern Germany, Right: Photo automatically taken during the flight over the power plant (top), dimensionless CO_2 profile scaling factors (middle), and dimensionless CH_4 profile scaling factors (bottom). All values shown in a given map as part of the flight have been scaled with a constant factor such that the scaled values of the whole flight are close to unity (green). The data have been smoothed using a seven point moving average. Gaps are due to the quality filtering (shown are only measurements where the spectral signal was larger than 3000 counts after dark signal correction and the root-mean-square (RMS) of the fit residuum (relative difference between measurement and model after the fit) is better than 1%). The CO_2 output of the power plant during the overflight was 56.6 t/min (personal communication Vattenfall Europe Generation AG & Co. KG, Cottbus, Germany, 2008).

AMTD
3, 3199–3276, 2010

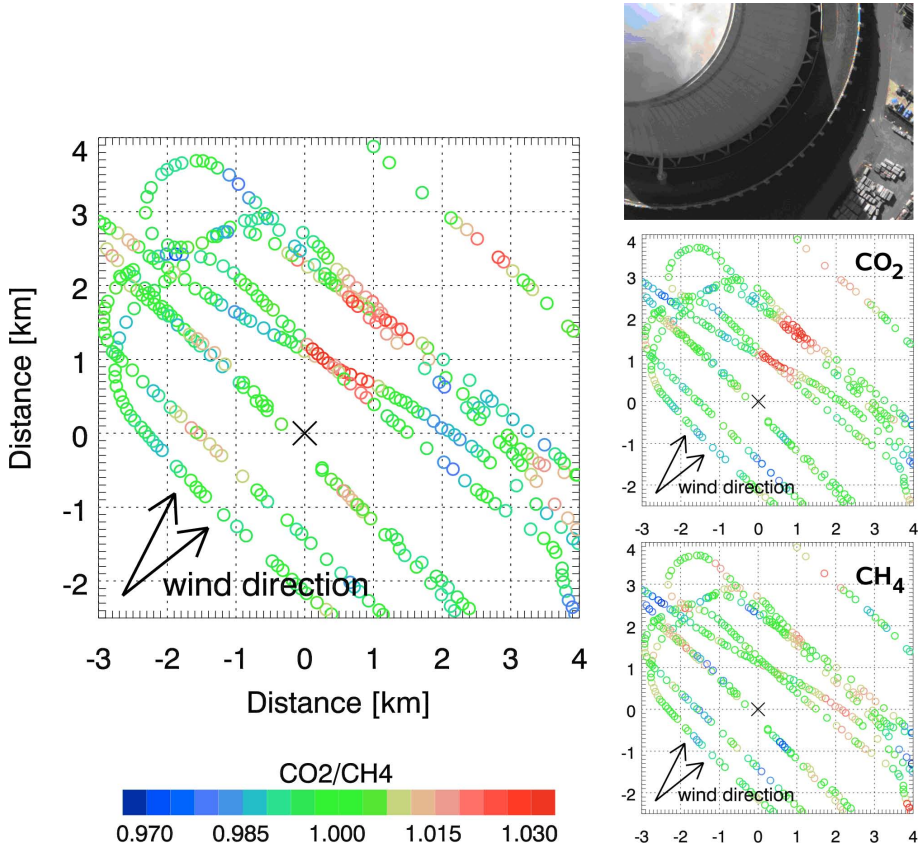

Fig. 13. As Fig. 12 but for the power plant Schwarze Pumpe located near the power plant Jänschwalde. The CO_2 output of the power plant was 26 t/min during the overflights (personal communication by Vattenfall Europe Generation AG & Co. KG, Cottbus, Germany, 2008).

AMTD
3, 3199–3276, 2010

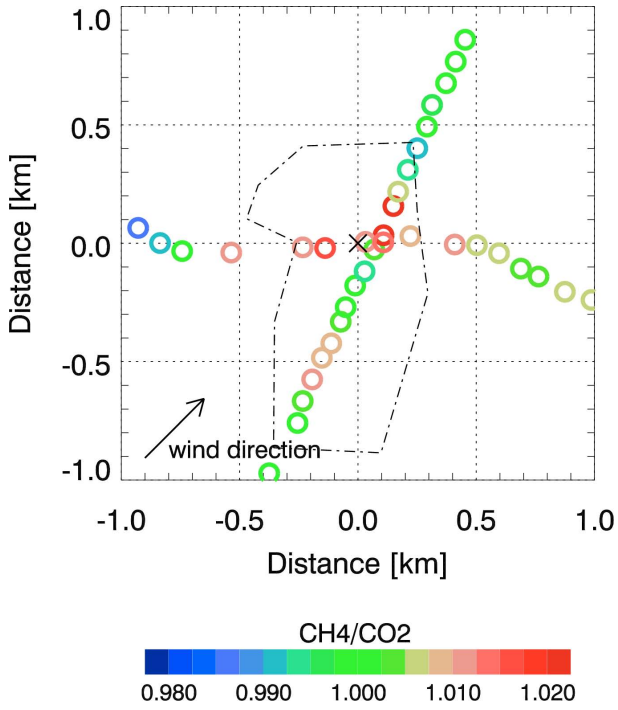

Fig. 14. Normalized CH_4/CO_2 profile scaling factor ratio ($PSFR_{BM}$) showing anomaly in the upper part of the landfill Vorketzin located near Berlin in Eastern Germany. Data acquired with MAMAP on 26 Jul 2007. The data have been smoothed using a three point moving average. Gaps are due to the quality filtering: Shown are only measurements where the spectral signal was larger than 3000 [BU] after dark signal correction and the root-mean-square (RMS) of the fit residuum (relative difference between measurement and model after the fit) is better than 1%. The dashed line shows the landfill body.

AMTD
3, 3199–3276, 2010